



Existence of chloride ions in high salinity wastewater accelerates the removal of micropollutants over light-driven catalysts

Cheng-Xin Chen^a, Shan-Shan Yang^{a,*}, Jie Ding^a, Lan Ding^b, Rui Wu^c, Lu-Ming Liu^c, Ji-Wei Pang^d, Lei He^a, Jun-Qiu Jiang^a, Nan-Qi Ren^a

^a State Key Laboratory of Urban Water Resource and Environment, School of Environment, Harbin Institute of Technology, Harbin 150090, China

^b College of Chemistry, Jilin University, 2699 Qianjin Street, Changchun 130012, China

^c Harbin Institute of Technology National Engineering Research Center of Water Resources Co., Ltd, Harbin 150090, China

^d China Energy Conservation and Environmental Protection Group, Beijing 100089, China

ARTICLE INFO

Keywords:

Anthraquinone
Radical
Electron transfer
Photoactivation
Chloride ions

ABSTRACT

Photocatalytic removal of micropollutants from highly saline water purification is challenging because of the interference and quenching of active species by chloride ions (Cl^-). Herein, anthraquinone-2-carboxylic acid (AQC) was anchored on aminated graphene sheets (AGR) to construct a metal-free photocatalyst (AQC/AGR) via a mild two-step method. We demonstrated efficient degradation of micropollutants on AQC/AGR, in which trimethoprim (TMP)-removal efficiency reached 97.7 % under solar irradiation for 40 min at high NaCl concentration (500 mM). A novel mechanism for the electron-transfer interaction of AQC/AGR with Cl^- and in situ generation of radicals from photoactivated Cl^- was explored through characterization measurements, radical quenching experiments and theoretical calculations. This system removed micropollutants mainly through radical processes mediated by superoxide radical ($\text{O}_2^{\cdot-}$), hydroxyl radical ($\cdot\text{OH}$) and dichloride radical anion ($\text{Cl}_2^{\cdot-}$). This work presents a novel family of catalysts for solar-energy-enabled removal of organic micropollutants to purify saline wastewater with high chloride concentration.

1. Introduction

Pharmaceuticals and personal care products (PPCPs)—such as antibiotics, non-steroidal anti-inflammatory drugs, and sunblock with persistent and recalcitrant properties—have detrimental effects on the ecosystem and human health and have aroused worldwide concern [1]. Advanced oxidation processes (AOPs) can produce highly reactive radicals, such as sulfate radical ($\text{SO}_4^{\cdot-}$), hydroxyl radical ($\cdot\text{OH}$), and superoxide radical ($\text{O}_2^{\cdot-}$), which can effectively destroy refractory organic contaminants [2]. Semiconductor photocatalysis and photosensitization are efficient, environment friendly, and cost-effective methods for degrading organic micropollutants in aquatic environments [3,4]. However, traditional semiconductor photocatalysts face interference from numerous inorganic salt ions [5]. Chloride ions with high ionic strength are ubiquitous in industrial effluents, seawater, and mariculture wastewater [5,6]. Moreover, Cl^- ions may considerably affect the degradation rate of PPCPs by blocking the active sites on the photocatalyst surface, scavenging the photogenerated active species (holes and $\cdot\text{OH}$), complexing with target pollutants, competing for photon

absorption, and functioning as a recombination promoter [7,8]. To the best of our knowledge, only a few studies have been conducted on eliminating organic pollutants from wastewater with high chloride ion content using photocatalysts under solar illumination [1,9–11].

The photoreactivity of anthraquinone (AQ) and its derivatives have attracted increasing interest. AQ molecules have been widely used as electron shuttles in the photocatalytic production of hydrogen peroxide (H_2O_2) [12], antibacterial agents for photoinduced sterilization [13], and organo-photocatalysts to synthesize high-value-added chemicals [14]. The inherent photosensitivity of AQ has led researchers to explore the possibility of its use in photocatalysis for contaminants removal and antibacterial effects [13,15]. Recent studies by our group have shown that the PPCPs can be effectively degraded in high chloride water by AQ-doped graphene under simulated solar irradiation [4,16]. Interestingly, solar irradiation of AQ in chloride-containing waters induces the production of reactive species such as excited triplet states of AQ ($^3\text{AQ}^*$), $^1\text{O}_2$, $\cdot\text{OH}$, $\text{O}_2^{\cdot-}$, chlorine radical (Cl^{\cdot}), and dichloride radical anion ($\text{Cl}_2^{\cdot-}$), which are crucial in the micropollutant removal process [4, 17–19]. Upon irradiation, $^3\text{AQ}^*$ can undergo electron-transfer reactions

* Corresponding author.

E-mail address: shanshanyang@hit.edu.cn (S.-S. Yang).

<https://doi.org/10.1016/j.apcatb.2023.122823>

Received 31 October 2022; Received in revised form 4 April 2023; Accepted 28 April 2023

Available online 29 April 2023

0926-3373/© 2023 Elsevier B.V. All rights reserved.

in high concentrations of chloride ions (act as electron donors), forming an AQ radical anion ($AQ^{\bullet-}$) and $Cl_2^{\bullet-}$ [19,20]. Reactive chlorine species (RCS, e.g., Cl^{\bullet} , $Cl_2^{\bullet-}$, or HOCl) and reactive oxygen species (ROS, e.g., $O_2^{\bullet-}$, $\bullet OH$, or H_2O_2) form in the subsequent radical chain reactions [20, 21]. The specific role of Cl^- in AQ-based photo-assisted degradation of organic pollutants has not been fully elucidated.

Notably, homogeneous photosensitive organic molecules face obstacles due to the following: low photosensitization efficiency, limited photostability, recombination of photogenerated carriers, and the risk of secondary contamination [22,23]. Therefore, implanting organic photosensitizers into the heterogeneous conductive supports provides a facile strategy to solve these hindrances [24,25]. Metal-free carbon-based materials, such as graphene oxide (GO) and reduced graphene oxide (rGO), have received considerable attention in photocatalytic applications [25,26]. The chemically modified GO has large oxygen-containing functional groups (such as quinone, carbonyl, and carboxyl), good electrical conductivity, high surface area, and adjustable electronic structure with delocalized π -electrons [27]. Introducing polar amine groups ($-NH_2$) to the surface of GO can increase the hydrophilicity and dispersion properties of graphene-based materials [28] and substantially impact the electronic structure without deconstructing the graphitic structure of graphene [29]. Nucleophilic substitution reactions can perform surface functionalization of GO by amine-containing molecules [30,31]. Amine-modified graphene has a wide range of applications in the adsorption and catalytic degradation of pollutants, synthesis of chemical products, and optoelectronic applications [28,32–35]. Furthermore, amine-functionalized graphene with a unique electronic structure facilitates the anchoring of functionalized compounds and enhances interfacial binding [36,37].

In this study, anthraquinone-2-carboxylic acid (AQC) was used as the model AQ molecule, and amine-functionalized graphene oxide (AGR) was selected to prepare the AQC-aminated graphene (AQC/AGR) composites using a two-step chemical grafting reaction. The performance of this prepared AQC/AGR with photocatalytic activation of Cl^- was evaluated for removing of PPCPs in abundant Cl^- conditions. The functionalization of organic materials on graphene is a feasible strategy for improving electronic conductivity and inhibiting the dissolution of photoactive molecules [25]. Hence, a possible photoactivated chloride ions mechanism was proposed for AQC/AGR-catalyzed photo-degradation of PPCPs in chloride-rich waters under solar irradiation.

2. Materials and methods

2.1. Chemicals and reagents

All chemicals and reagents used in the experiment were of analytical grade and were used without further purification. Detailed information is described in Text S1.

2.2. Synthesis of catalysts

The AQC/AGR photocatalyst was obtained via a facile two-step self-assembly fabrication route. First, the reported method prepared the aminated graphene oxide (AGR) with slight modification [38]. Specifically, 0.2 g GO was added to 100 mL deionized water (DW) and ultrasonically exfoliated to form a uniform solution. 1 mL $NH_3 \cdot H_2O$ was added to the above solution to adjust pH to 9–10. Subsequently, the mixture was heated in a water bath and continuously stirred. When the temperature reached 98 °C, 6 mL diethylenetriamine (DETA) was added and stirred for another six h. Afterward, thus obtained AGR was washed with DW to remove impurities and vacuum dried at 60 °C for 24 h.

The procedure for synthesizing AQC/AGR composites is as follows: appropriate amounts of AQC were dissolved in 100 mL of water. An aqueous dispersion of AGR was added to the AQC solution, and the resulting mixture was stirred at 80 °C for 12 h in a water bath. The final product was washed with DW to remove the excess AQC and vacuum

dried at 60 °C for 24 h. Six different AQC to AGR precursor ratios viz. 25 %, 50 %, 75 %, 100 %, 125 %, and 150 % were used to prepare respective AQC/AGRs and labeled as AQC/AGR-0.25, AQC/AGR-0.5, AQC/AGR-0.75, AQC/AGR-1, AQC/AGR-1.25, and AQC/AGR-1.5, respectively. For example, during AQC/AGR-1 synthesis, 100 mg AQC was mixed with 100 mg AGR precursor, and the rest of the combinations were prepared similarly.

2.3. Characterization

The morphologies and microstructures of the as-prepared samples were investigated by scanning electron microscopy (SEM, Zeiss Sigma 300, Germany) and transmission electron microscopy (TEM, JOEL JEM-F200, Japan). The phase structure and crystallinity of the composites were identified by analyzing the X-ray diffraction (XRD) patterns obtained from an X-ray diffractometer with Cu K α radiation (Philip X'Pert pro, Netherlands). The surface functional groups of the samples were determined using a Fourier transform infrared spectrometer (FTIR, Thermo Scientific Nicolet is50, USA) in the range of 4000–400 cm^{-1} . Raman spectra of the samples were recorded on a Raman spectrometer upon excitation with a 532 nm laser (inVia-Reflex, Renishaw, England). Thermogravimetric analysis (TGA) of the as-prepared samples was conducted on a thermogravimetric analyzer (TGA5500, TA instruments, USA) at a heating rate of 10 °C /min from 20 °C to 800 °C under an N_2 atmosphere. The elemental composition and chemical nature of the surface of AQC/AGR were identified with X-ray photoelectron spectroscopy (XPS, ESCALAB 250Xi, ThermoFisher, USA) with an Al K α X-ray source. The samples' specific surface area and pore size distribution were measured using an N_2 adsorption-desorption apparatus (ASAP 2460, Micromeritics, USA). The zeta potential values of AQC/AGR-1 were measured using the zeta potential analyzer (Malvern Zetasizer Nano ZS90, UK).

To evaluate the optical property of the photocatalyst, UV-visible diffuse reflectance (UV-vis DRS) spectra were obtained using a UV-vis spectrophotometer (Shimadzu, UV-2550 spectrophotometer, Japan). The optical band gap energies for AQC and AQC/AGR can be obtained using the Tauc approach according to Eq. (1).

$$\alpha h\nu = A (h\nu - E_g)^{n/2} \quad (1)$$

where α , h , ν , A , E_g , and n are the absorption coefficient, Planck's constant, incident light frequency, constant, and bandgap respectively and n value is 1. The extinction, diffuse reflectance and diffuse transmittance measurements of the AQC-AGR suspensions were performed on a spectroradiometer (PerkinElmer Lambda950, USA). For diffuse reflectance and diffuse transmittance measurements, an integrating sphere reflectance attachment was used [39]. All measurements were performed in the range of 300–800 nm. The rectangular quartz cuvette is 1 mm in length. The catalysts were ultrasonically dispersed in deionized water to prepare suspensions of different concentrations. The calculations were performed assuming solar irradiance (320 nm–780 nm) on a surface tilted at 37° to the sun [40]. The photoluminescence (PL) spectra were acquired using a fluorescence spectrophotometer (HITACHI F-7100, Japan). The photoelectrochemical measurements, including transient photocurrent response, electrochemical impedance spectroscopy (EIS), and Mott–Schottky (M-S) plots, were carried out on an electrochemical station (CHI 660E, CH Instrument, China) using a standard three-electrode system. The catalyst dip-coated Indium tin oxide (ITO) glass, Ag/AgCl electrode, and platinum (Pt) plate served as the working electrode, reference electrode, and counter electrode. An aqueous Na_2SO_4 solution (0.2 M, pH = 6.8) was used as the electrolyte solution. A 300 W Xenon lamp was used as the intermittent light source. EIS measurements were performed from 0.1 Hz to 10 kHz. M-S analysis was performed at the frequency of 1500 Hz. Cyclic voltammetry (CV) measurements were performed at a scanning rate of 0.1 $V s^{-1}$.

2.4. Photocatalytic performance evaluation

The photocatalytic activity and recyclability of AQC/AGR composites were evaluated towards the degradation of PPCPs. Explicitly, 5 mg of the photocatalyst was added to 100 mL of 10 mg/L PPCPs solution. The mixture was stirred in the dark for 30 min to establish the adsorption-desorption equilibrium. Afterward, the solution was irradiated with a Xenon lamp (300 W, PLS-SXE 300UV, Beijing Perfectlight Co., Ltd.) equipped with an AM 1.5 G filter ($320\text{ nm} \leq \lambda \leq 780\text{ nm}$). During the illumination period, 1 mL of samples were withdrawn at specific intervals and filtered through a $0.22\text{ }\mu\text{m}$ filter. Next, the filtrate was immediately mixed with $20\text{ }\mu\text{L}$ $\text{Na}_2\text{S}_2\text{O}_3$ (1 mol/L) for concentration determination. During the photocatalytic process, the temperature was maintained at $25 \pm 1\text{ }^\circ\text{C}$ via a circulating water bath, and the initial pH of the solution was adjusted to a pre-determined value by 0.1 M H_2SO_4 and 0.1 M NaOH. All the experiments were conducted at least in duplicate. A detailed description of the photoreaction system is provided in Text S2.

Recycling experiments determined the AQC/AGR photocatalyst's recyclability. Concisely, the used photocatalyst was recovered by vacuum filtration, washed with DW, and dried overnight at $60\text{ }^\circ\text{C}$. The collected photocatalyst was reused under the same reaction conditions as described earlier.

The kinetic data of photodegradation were fitted with the pseudo-first-order kinetic model described by Eq. (2).

$$-\ln(C_t/C_0) = k_{\text{obs}} t \quad (2)$$

where C_t is the concentration of contaminants solution (mg/L) at time t , C_0 is the initial concentration of contaminants before irradiation, t is the reaction time (min), and k_{obs} is the pseudo-first-order kinetic rate constant (min^{-1}).

2.5. Analytic methods

The concentrations of PPCPs were determined by UV-vis spectrophotometer and ultrahigh-performance liquid chromatography (UPLC, Waters e2695, USA) with a photodiode array detector (PDA). Byproducts formed during the TMP degradation were characterized by high-

performance liquid chromatography-tandem quadrupole time-flight mass spectrometry (HPLC/Q-TOF-MS), and the toxicity of byproducts was estimated by Toxicity Estimation Software Tool (T.E.S.T.). The toxicity of TMP and its degradation intermediates are listed in Table S11. The disinfection byproducts (DBPs) were determined by gas chromatograph-mass spectrometry (GC-MS, QP2020NX, Shimadzu, Japan). Radical-scavenging experiments and EPR measurements determined the generated active species. Details of the aforementioned analytic methods and instruments are provided in Text S3.

2.6. DFT calculations

The quantum chemistry calculations were conducted based on Density functional theory (DFT) using the Gaussian program to reveal the reactive sites of TMP [41]. Spin population analysis of AQC in triplet excited states with Cl^- using Gaussian 16. The AQC/AGR model and AQC/AGR adsorbed chloride ions (AQC/AGR-Cl) model were performed using the Vienna ab initio Simulation package (VASP) [42]. Detailed information on DFT calculations is supplied in Text S4.

3. Results and discussion

3.1. Morphological and structural analysis

The synthetic scheme of AQC/AGR composites is illustrated in Fig. 1a. GO nanosheets have an affinity with amine-containing substances (such as DETA) due to the abundance of oxygen-containing functional groups ($-\text{OH}$, $-\text{COOH}$, $\text{C}-\text{O}-\text{C}$) and versatile sites on their surface [43]. Diethylenetriamine (DETA) serves as a reducing agent and surface modifier by reacting with the epoxy groups of GO through nucleophilic ring-opening reactions [30,44]. The amine-functionalized graphene enhances the interfacial bonding with organic functional molecules. GO is modified by DETA to form positive charges through amino protonation. The electrostatic self-assembly may be triggered when oppositely charged anthraquinone-2-carboxylic acid and the positively charged aminated graphene [45]. Graphene composed of a π -conjugated system can bind to organic molecules containing benzene rings via π - π interaction [46]. Overall, self-assembled AQC-functionalized graphene sheets are formed due to

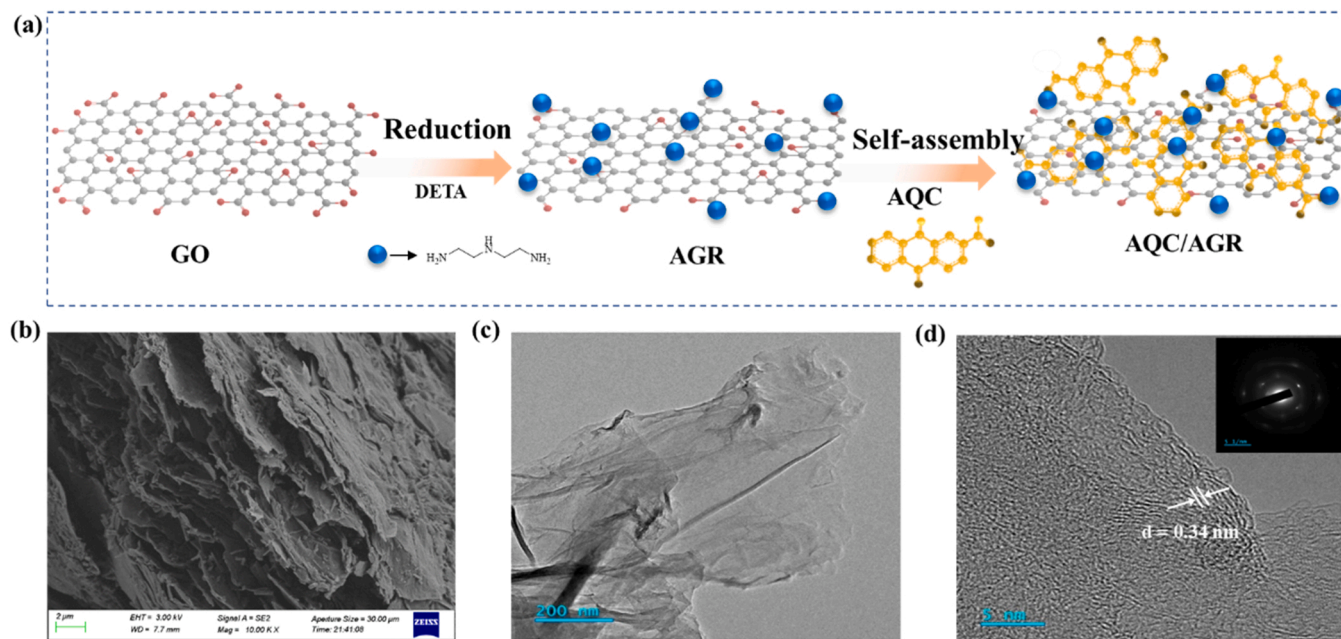


Fig. 1. (a) Schematic showing the synthesis of the AQC/AGR composites (here the blue ball represents DETA). (b) SEM image of AQC/AGR-1. (c, d) TEM images of AQC/AGR-1. The inset in (d) is the selected area electron diffraction (SAED) pattern.

the π - π stacking interaction owing to the aromatic structure of AQC and delocalized π -electrons of AGR, electrostatic interaction, and hydrogen bonding [12,25]. The SEM analysis of pure AQC revealed a disordered appearance without distinct nanostructures (Fig. S1a). Compared to bare GO with smooth stacked sheets (Fig. S1b), AGR shows a curled morphology due to the disruption of the carbon skeleton and loss of long-range ordering caused by the reducing agent DETA (Fig. S1c) [45, 47]. Interestingly, AQC/AGR-1 exhibits an ordered compacted sheet structure with layer-by-layer self-assembly (Fig. 1b). The TEM image exhibits a wrinkled nanoplatelet-like structure of AQC/AGR without apparent agglomeration (Fig. 1c) [46]. A regular lattice of graphene was observed. The d-spacing values were calculated to be around 0.34 nm, assigned to the (002) lattice plane of graphene (Fig. 1d). The selected area electron diffraction (SAED) image shows a typical 6-fold symmetric diffraction (Fig. 1d, inset) corresponding to the hexagonal carbon rings and graphite planes, verifying the high crystallinity of graphene [48]. The blurred halo background is attributed to weak π - π interactions between graphene and AQC [49].

XRD pattern of GO exhibits a peak at $2\theta = 12.7^\circ$, corresponding to the (001) plane of graphite (Fig. 2a). AGR and AQC/AGR composites have a broad diffraction peak appears at $\sim 24.2^\circ$, attributing to the

interlayer π - π stacking of graphene (002) plane [50], and (001) plane disappears due to the reduction by DETA. Noteworthy that the (002) plane of AQC/AGR shifts to higher 2θ and becomes sharp, corresponding to the decrease of interplanar spacing and the high crystalline structure, presumably because of the introduction of AQC and the reconstruction of the carbon skeleton of graphene sheets, which is consistent with the SEM observations. Moreover, as presented in Fig. S2a, two prominent peaks of AQC/AGR originating from AQC appeared when the mass ratio was increased (0.75, 1, and 1.25), implying that the AQC was successfully coupled with graphene.

According to the FTIR, the oxygen-containing peaks become weaker in AGR as compared to GO, while a sharp peak at 1193 cm^{-1} (C—N stretching) and a broad and small peak at 3400 cm^{-1} (N—H stretching) appeared, indicating the reduction of GO and the introduction of amine groups (Fig. 2b). In addition, an intense peak at 1560 cm^{-1} in AGR is ascribed to the stacking of the C=C and N—H bonds [32]. The C=O peak of AQC is red-shifted from 1692 cm^{-1} to 1676 cm^{-1} for the C=O bond of AQC/AGR-1. Moreover, the C—N peak at 1190 cm^{-1} in AGR was red-shifted to 1172 cm^{-1} in AQC/AGR-1, implying that the intense interfacial interaction arising from electron delocalization facilitated the electron transfer between AQC and graphene [51]. As shown in Fig. S2b,

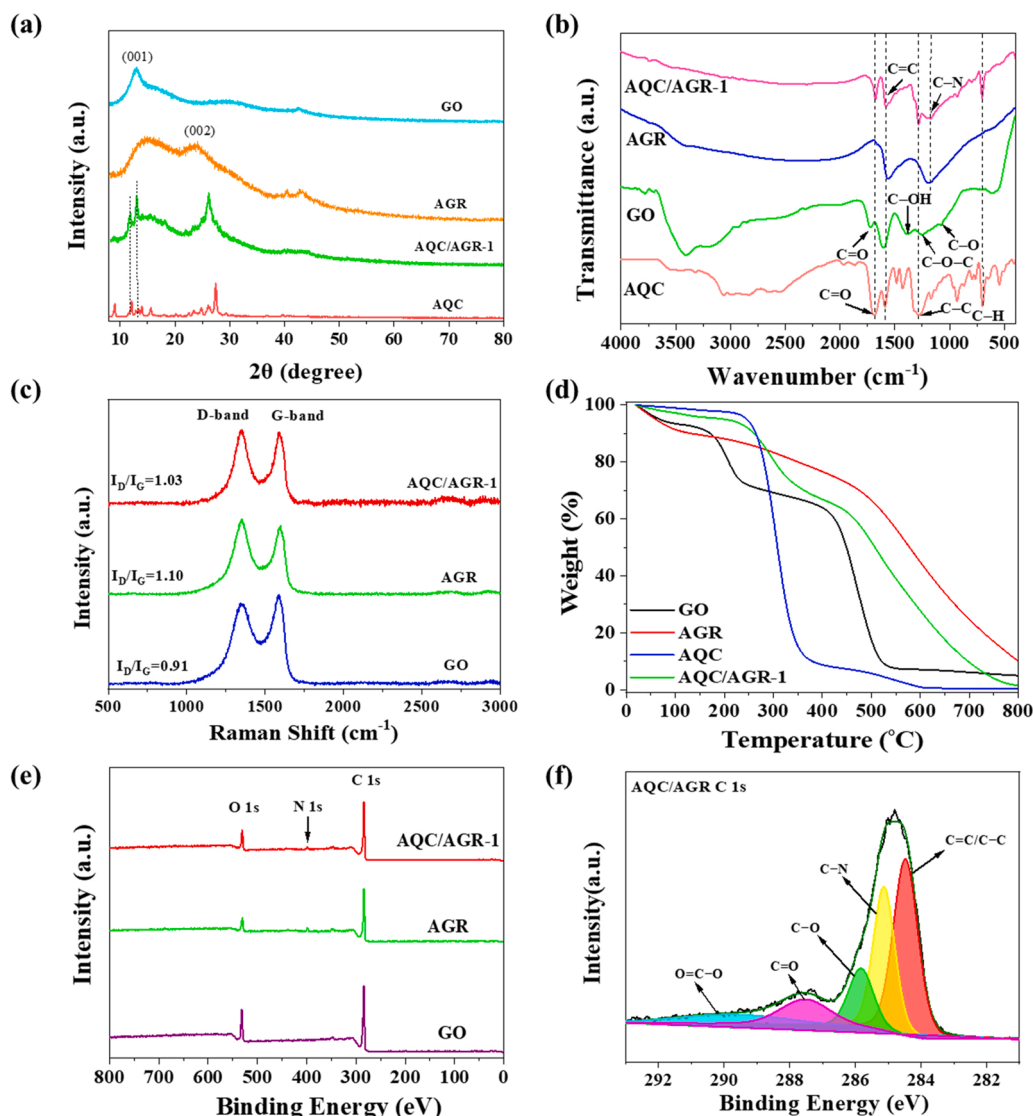


Fig. 2. (a) XRD patterns of AQC, GO, AGR, and AQC/AGR-1. (b) FTIR spectra of the AQC, GO, AGR, and AQC/AGR-1 samples. (c) Raman spectra of GO, AGR, and AQC/AGR-1. (d) TGA curves of AQC, GO, AGR, and AQC/AGR-1. (e) Survey XPS spectra of GO, AGR, and AQC/AGR-1. (f) High-resolution XPS C 1s spectra of AQC/AGR-1.

other characteristic peaks of AQC ($\sim 1280\text{ cm}^{-1}$, C—C stretching; 700 cm^{-1} , out-of-plane C—H bending) become unambiguous in AQC/AGR composites with a higher AQC to AGR mass ratio, indicating the successful incorporation of AQC onto the graphene framework [52].

Raman spectra of the samples exhibited distinct D and G bands at ~ 1347 and $\sim 1587\text{ cm}^{-1}$, respectively (Fig. 2c). The intensity ratio of the D to G band (I_D/I_G) increased to 1.10 after amine functionalization, indicating the decrease of the graphitic domains. Surprisingly, after the modification with AQC, the I_D/I_G ratio of the AQC/AGR composites gradually decreased with the increasing AQC to AGR mass ratio (Fig. S2c), suggesting that modification with organic materials restored the partial sp^2 conjugated system or the overlap with the C=C vibrations of quinones on the surface of graphene [25,46]. Hence, this preparation strategy with strong bonding interactions does not considerably disturb the structure of graphene.

According to the TGA curves (Fig. 2d), AGR showed better thermal stability than GO at temperatures above 200°C , owing to the removal of thermally labile groups on the surface of GO. Pure AQC exhibits a large portion of weight loss between 230 and 400°C , possibly due to the carbonization of AQC molecules, whereas AGR lost only 11.08 % of its weight in this temperature range. These results suggest that most of the weight loss exhibited by AQC/AGR-1 in this temperature interval may be due to the thermal degradation of AQC coating in the composite sheet structure [52].

From the XPS survey spectra (Fig. 2e), C and O elements were observed for GO, while the peaks of C, N, and O elements were detected for AQC/AGR-1 and AGR. Compared with GO, the elemental N content of AGR increased, and the O element decreased after amination, confirming the successful reduction and amine functionalization of GO, while the O content on the surface of AQC/AGR-1 has increased after AQC anchoring compared to AGR (Table S2). GO's high-resolution C 1s spectra can be fitted using the five featured components. The typical peaks at 284.6 eV, 285.3 eV, 286.5 eV, and 288.2 eV were attributed to C=C/C—C, C—O, C=O, and O=C—O, respectively (Fig. S3a). In high-resolution O 1s spectra of GO, the peaks at 531.5 eV, 532.4 eV, 533.1 eV, and 534.0 eV contributed to the functional groups of C=O, surface adsorbed H_2O or O_2 , O—C, and O=C=O, respectively (Fig. S3b). Upon chemical reduction, the peaks corresponding to O—C and O=C—O in AGR and AQC/AGR-1 showed a weaker intensity than GO (Fig. S3d and f). This is consistent with the observations of FTIR. Compared with GO, the intensity of the peaks of oxygenous groups of AQC/AGR-1 decreased, and the new peak appearing at 285.1 eV corresponds to C—N (Fig. 2f). The N 1s spectra for AQC/AGR-1 showed the binding energy at 399.6 eV, which was assigned to C—N (Fig. S3e). This is due to the chemical reduction of GO and the functionalization of amine groups. The C=C/C—C and C—N binding energies of AQC/AGR-1 are lower than that of AGR (Fig. S3c), suggesting that the hybridization effect between AQC and AGR increased the electron density of AQC/AGR-1.

AQC/AGR-1 exhibited a reduced specific surface area (SSA) than AGR because the AQC covering on the graphene sheets surface probably decreased SSA (Table S2) [25]. The decline in the pore volume of AQC/AGR-1 may likely result in the reduced nanosheet layer spacing, which is consistent with the SEM and XRD observations [53]. The mesopore pore size distribution of AQC/AGR-1 was obtained to be 2–10 nm, which is beneficial to the rapid transport of Cl^- and electrons (Fig. S4). The aggregation of pristine graphene leads to the reduction of effective mass diffusion pathways and surface area [54]. However, the reduction of oxygen-containing functional groups and functionalization on the GO surface can reduce the aggregation of graphene. A high specific surface area and porous structure on the catalyst's surface could provide more active sites and numerous boundaries conducive to the enrichment and diffusion of pollutants/ions, and mass transfer during the photocatalytic process [55–57]. The wrinkled and pore structure can also enhance the adsorption of organic pollutants by graphene nanosheets [58]. The open sheet arrangement provides more accessible surfaces and easy pathways facilitating contact with reactants [59].

3.2. Photocatalytic performance over AQC/AGR

Trimethoprim (TMP) is synergistically used with sulfonamides to treat infectious diseases in humans and animals and is also used as a feed additive in the livestock industry [60]. The photocatalytic performance of as-prepared samples was evaluated towards the degradation of TMP, which is frequently detected in natural water sources and poses risks to the aquatic ecosystem. Photolysis of TMP is negligible, regardless of the presence of NaCl, under solar irradiation (Fig. 3a). The adsorption capacity of AQC/AGR-1 led to negligible TMP removal under dark conditions. In addition, the solar-irradiation-excited AQC/AGR-1 cannot effectively catalyze TMP degradation without NaCl. Interestingly, AQC/AGR-1 exhibited a splendid photocatalytic performance in the presence of 500 mM NaCl, where 97.7 % TMP was degraded upon solar irradiation after 40 min, indicating the efficient activation of Cl^- over AQC/AGR-1 for pollutants abatement. To determine the positive effect of Cl^- on the photodegradation of TMP, rather than the effect of ionic strength, the effect of inert sodium salt (NaClO_4 , 500 mM; Na_2SO_4 , 167 mM) was subsequently investigated. The almost negligible TMP degradation rate was observed in the presence of NaClO_4 alone (Fig. 3b), signifying that Cl^- can accelerate the degradation efficiency of TMP. The general process of activation of chloride ions by light-driven catalysts to produce radicals is described in Text S5. After that, several representative micropollutants were selected to test the application of AQC/AGR photocatalytic activation of the chloride ions system. These include sulfamethoxazole (SMX), sulfadiazine (SDZ), norfloxacin (NOR), chlortetracycline hydrochloride (CTC), diclofenac (DCF) and reactive red 2 (RR2). AQC/AGR-1 exhibited excellent photocatalytic abatement towards these micropollutants (Fig. 3c), and the difference in reaction rate depends mainly on the electron-donating or withdrawing properties in the structures of the contaminants [61]. From the core structure, the difference in the structures of different contaminants may significantly affect on the respective degradation activity, reactive site, and pathway. Generally, organic pollutants with electron-donating groups are more easily oxidated than electron-withdrawing groups [62]. The selective reactivity of ROS and RCS and the active sites being attacked in the system differ for contaminants with different molecular structures. In contrast to non-selective $\cdot\text{OH}$, halogen radicals (e.g., $\text{Cl}\cdot$ and $\text{Cl}_2\cdot^-$) can selectively degrade substrates and preferentially react with electron-rich organic compounds, including phenols, sulfides, and amines, with some compounds even more reactive than $\cdot\text{OH}$ [21]. $\text{Cl}\cdot$ and $\text{Cl}_2\cdot^-$ can react rapidly with many organic compounds with electron-donating substituents, such as sulfonamides, tetracyclines, fluoroquinolones, and trimethoprim ($k = 10^8\text{--}10^{10}\text{ M}^{-1}\text{ s}^{-1}$) [61,63]. $\text{Cl}\cdot$ and $\text{Cl}_2\cdot^-$ can react with substrates via single electron transfer (SET), H-abstraction, and addition pathways, where SET is the primary reaction mechanism with pollutants bearing phenol, alkoxy benzene, and aniline groups [61]. In treating of brine with high chloride concentration (500 mM), $\text{Cl}_2\cdot^-$ plays a prominent role in the degradation of some pollutants. The analysis of the possible sites of different pollutants attacked by radicals is presented in Text S6. The differences in the degradation effects of micropollutants with different structures will be the focus of further research.

The effect of the amount of AQC in the AQC/AGR composites was investigated; the direct photocatalytic influence of pristine AGR (without photoactive component loading) can be neglected (Fig. 3d). After functionalizing AGR with AQC, the degradation efficiency of AQC/AGR for TMP increased from 16.9 % to 97.7 % with the increase in the content of AQC from 25 % to 100 %. Moreover, the rate constants also increased from 0.0031 min^{-1} to 0.094 min^{-1} (Table S3). However, any further increase in the content of photosensitive AQC slightly decreased the photocatalytic activity, which may be attributed to the coverage of active sites of AQC/AGR and self-quenching of the excited material. Therefore, the AQC/AGR-1 exhibited the optimal catalytic performance among all the samples.

The effect of the amount of catalyst on the degradation of TMP was

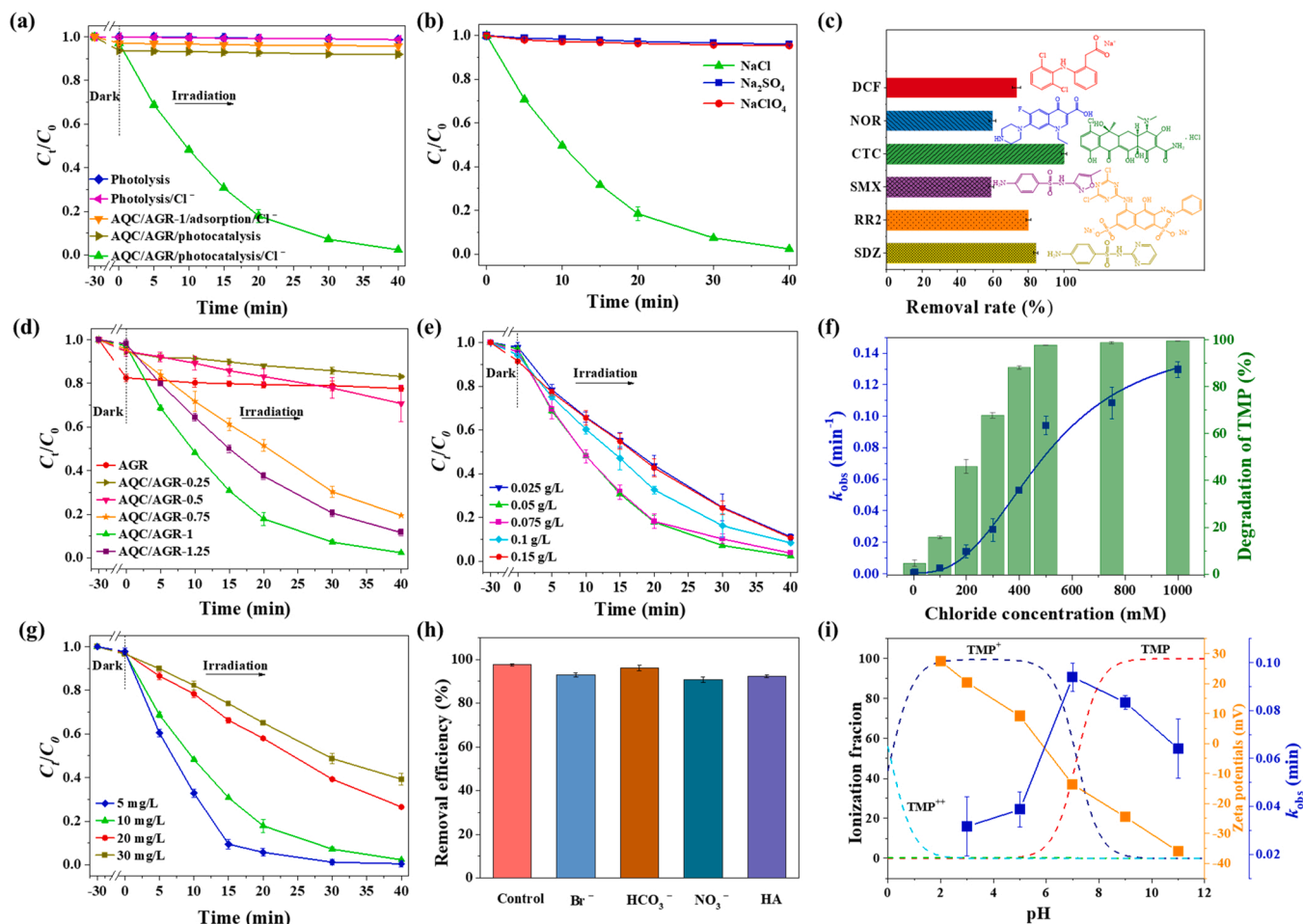


Fig. 3. (a) Degradation of TMP by photolysis, AQC/AGR-1 adsorption, and AQC/AGR-1 photocatalysis under solar light irradiation in the presence of NaCl (500 mM) or not. (b) The effect of different sodium salts on photocatalytic activity of AQC/AGR-1 (e.g., [NaCl] = 500 mM, [Na₂SO₄] = 167 mM, and [NaClO₄] = 500 mM). (c) Removal efficiency for photocatalytic degradation of several contaminants by solar-activated AQC/AGR. In all cases, the initial concentration of contaminants was 10 mg/L ([AQC/AGR] = 50 mg/L, [NaCl] = 500 mM, initial pH = 7.0, and error bars indicate one standard deviation). (d) Comparison of TMP removal by AQC/AGR samples with different mass ratios under solar irradiation. (e) Comparison of TMP removal by AQC/AGR-1 with different catalyst dosages under solar irradiation. (f) Rate constant k_{obs} and TMP removal under different NaCl concentration. (g) Comparison of TMP removal by AQC/AGR-1 with different initial TMP concentration under solar irradiation. (h) Comparison of TMP removal by AQC/AGR-1 in the presence of 500 mM NaCl and co-exist water substances (e.g., [Br⁻] = 0.8 mM, [HCO₃⁻] = 2.3 mM, [NO₃⁻] = 1 mM, and [HA] = 0.5 mg/L). (i) Rate constants for TMP photocatalysis in the AQC/AGR-1 system in the presence of 500 mM NaCl (primary y axis, red bar) and the zeta potentials (secondary y axis, gray bar) as a function of solution pH.

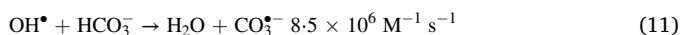
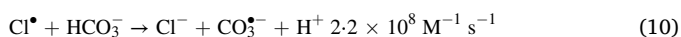
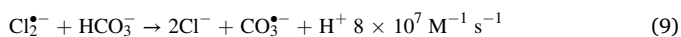
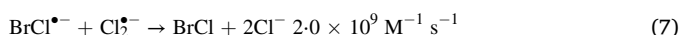
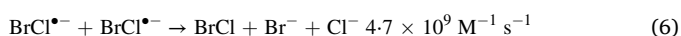
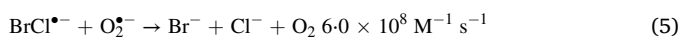
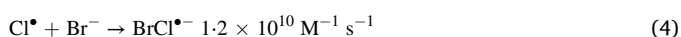
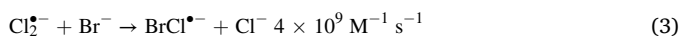
investigated by varying the amount of AQC/AGR composite (Fig. 3e). The TMP degradation values of 88.9 %, 97.7 %, 96.4 %, 91.7 %, and 89.4 % were obtained at 40 min for the catalyst amounts of 0.025, 0.05, 0.075, 0.1, and 0.125 g/L, respectively. The increasing catalyst dose can increase the active species through Cl⁻ activation in the reaction system. Moreover, when the catalyst dosage increases, the accumulated solution turbidity would hinder light transmission, thus delaying TMP's effective degradation [64,65]. And the catalyst aggregation may become a new recombination center of photogenerated carriers via non-radiative transitions or quench the exciplex depending on the concentration of photoactive centers, while also affecting the optical properties of the catalyst [17,66–68].

The TMP removal rate constant increased from 0.005 to 0.094 min⁻¹ upon increasing the NaCl concentration from 0 to 500 mM (Fig. 3f and Table S5). The light-driven AQ-based catalyst forms a charge transfer exciplex with chloride ions, dissociating more readily to generate active species at high Cl⁻ concentrations (Eqs. S5–S7, Text S5). The high NaCl concentrations can enhance the generation of strong, active species, further promoting TMP abatement. The increasing trend of the degradation rate constants of TMP diminished when the NaCl concentration increased to 1000 mM ($k = 0.1296$ min⁻¹). This phenomenon may be

due to the limited availability of the active sites on the catalyst or the mutual quenching of co-occurring radicals (Eqs. S8–S11), ultimately affecting the efficiency of photocatalysis. As shown in Fig. 3g, the removal percentage of TMP gradually decreased with the increase in the initial concentration of TMP from 5 to 30 mg/L. The observed rate constants also decreased from 0.1522 to 0.0234 min⁻¹ (Table S6). This decrease may have been due to the insufficient reactive sites on AQC/AGR.

A superior photocatalyst should have resistance to environmental interference. Dissolved organic matter (DOM) and various anions, including NO₃⁻, HCO₃⁻, and Br⁻, are ubiquitous in natural seawater and saline wastewater and may function as radical promoters or scavengers, thereby facilitating or inhibiting the transformation kinetics of micropollutants. The effects of these water matrices on the photocatalytic removal of TMP are discussed here. The degradation rate of TMP was slightly affected in the presence of Br⁻ and 500 mM NaCl (Fig. 3h). Using 0.8 mM Br⁻ in the presence of 500 mM NaClO₄ had a negligible effect on the photocatalytic removal of pollutants (Fig. S5a), suggesting that low concentrations of Br⁻ favor exciplex quenching over the formation of reactive species. Furthermore, Br⁻ can react with chlorine radicals to form BrCl[•] and continue to react with other radicals or

undergo self-quenching (Eqs. 3–7). Therefore, Br^- exciplexes may also promote RCS (such as $\text{BrCl}^{\bullet-}$) formation according to Eq. (8), where Cl^- concentrations are 625-fold higher than Br^- [69]. It is assumed that the rate constant for the formation of $\text{BrCl}^{\bullet-}$ is similar to that of mono-halogen radicals. Here, the reduction potentials of Br^\bullet and Cl^\bullet are 1.92 V_{NHE} and 2.50 V_{NHE} , respectively [20,69]. As illustrated in Fig. 3h, the removal rate of TMP in the presence of 0 and 2 mM HCO_3^- concentrations were 97.7 % and 96.2 %, respectively. HCO_3^- can scavenge reactive species to form carbonate radical ($\text{CO}_3^{\bullet-}$, $E = 1.59 V_{\text{NHE}}$) with a low oxidizing capability (Eqs. 9–11) [70]. As a highly selective secondary radical, $\text{CO}_3^{\bullet-}$ has been reported to react rapidly with organic contaminants containing electron-rich groups, such as aniline and phenolic hydroxyl groups [71,72]. The potentially high reactivity of $\text{CO}_3^{\bullet-}$ with TMP has also been reported in the literature [71,73]. The minor inhibitory impact of NO_3^- may be mainly due to the scavenging of photogenerated electrons by reacting with NO_3^- , thus acting as an electron scavenger [74–79].



As a typical component of NOM, humic acid (HA) at two different concentration levels was used to explore its effect on the degradation of TMP. In the presence of HA (0.5 mg/L), the removal rate of TMP decreased to 92.5 %. As shown in Fig. S5b, upon increasing the HA concentration from 0.5 to 5 mg/L, the degradation efficiency decreased from 92.5 % to 27.9 %. In addition, NOM mainly competes in reactions involving reactive species, quenches excited states of photosensitive substances, and covers the active sites of the catalyst, thus adversely impacting the photocatalytic performance [80,81]. HA has high aromaticity and electron-rich moieties, to which RHS (e.g., Cl^\bullet and $\text{Cl}_2^{\bullet-}$) are prone to react via electron abstraction or the chlorine addition reaction. The reported second-order rate constant of the reactions of RHS with various HA concentrations lay within the range of $2.61 \times 10^7 \text{ M}^{-1} \text{ s}^{-1}$ to $5.3 \times 10^8 \text{ M}^{-1} \text{ s}^{-1}$ [82]. Although HCO_3^- , Br^- , NO_3^- , and HA have slightly weakening effects on the transformation kinetics of TMP in the presence of Cl^- , the photocatalytic efficiency remains appreciable. These results imply that AQC/AGR-1 has an excellent ability for anti-anion interference in micropollutant removal.

Fig. 3i exhibits the effect of initial pH on the degradation of TMP in water containing 500 mM Cl^- . AQC/AGR showed a favorable TMP removal efficiency within a wide range of pH (3–11), suggesting the suitability of AQC/AGR under the studied environmental conditions. The pseudo-first-order kinetic constants were determined to be 0.0356, 0.0381, 0.094, 0.0834, and 0.0612 min^{-1} at 3, 5, 7, 9 and 11 pH values, respectively (Table S7). The variation of catalytic efficiencies with pH values could be explained by the electrostatic attraction/repulsion between the surface of the catalyst and TMP and the competitive consumption of various radical species. TMP exists in three forms TMP^{++} , TMP^+ , and TMP [60]. In addition, the pK_a values were calculated using Marvin Sketch software from ChemAxon (<https://www.chemaxon.com>), and the speciation of TMP is presented in Fig. 3i ($\text{pK}_{a1} = 0.1$, $\text{pK}_{a2} = 7.16$). The surface of AQC/AGR exhibited positive zeta potentials with

an isoelectric point of 5.75 under acidic conditions (Fig. 3i), and both the photocatalyst and TMP were positively charged. Therefore, electrostatic repulsion is an essential factor affecting the photocatalytic efficiency of AQC/AGR under acidic conditions. Under neutral conditions, TMP existed in non-protonated neutral form and TMP^+ . The highest rate constant at the pH of 7 can be attributed to the negatively charged AQC/AGR catalyst that facilitated the adsorption of positively charged TMP (TMP^+) on its surface. The impact of pH on the degradation rate of TMP could also be explained by the reaction rate between TMP and HOCl/OCl^- ($\text{pK}_a = 7.5$) [60]. The neutral TMP was more nucleophilic and reactive among the acid–base species of TMP and displayed the highest rate constant with HOCl ($1.6 \times 10^2 \text{ M}^{-1} \text{ s}^{-1}$) [60]. The rate constant of TMP^+ and HOCl was considerably small ($6.2 \text{ M}^{-1} \text{ s}^{-1}$), and the reactions of OCl^- with TMP were negligible [60,71]. Furthermore, $\text{O}_2^{\bullet-}$ could be quenched through excess H^+ , forming HO_2^\bullet ($\text{pK}_a = 4.8$), and $\text{Cl}_2^{\bullet-}$ and HO_2^\bullet are more likely to undergo mutual consumption under acidic conditions than $\text{O}_2^{\bullet-}$ (Eq. S12) [4]. Additionally, Cl^\bullet and $\text{Cl}_2^{\bullet-}$ were consumed by OH^- and formed less-active radicals under alkaline conditions, and thus the solution pH decreased slightly (Eqs. S13 and S14, Fig. S5c). The other optimal conditions for AQC/AGR photocatalyzed degradation of TMP are a catalyst dosage of 0.05 g/L, and an initial pH value of 7, wherein the mineralization efficiency of the reaction system was 49.1 % by measurement of total organic carbon (TOC) (Fig. S5d).

The reusability of nanocomposites is essential for their practical applications. As shown in Fig. 4a, the used AQC/AGR exhibited outstanding recyclability and stability even after five cycles, where a removal rate of 86.22 % for TMP was obtained after the fifth cycle. The slight decrease in the removal efficiency is due to the unavoidable catalyst loss in the recovery process. Compared with the fresh AQC/AGR, no noticeable morphological and structural changes were observed during the SEM, XRD, FTIR, Raman, and XPS analyses (Fig. 4b–f), thus demonstrating the excellent catalytic activity and structural stability of the composite, manifesting high availability for practical applications. In addition, by analyzing the O 1s high-resolution XPS spectra of fresh AQC/AGR and used AQC/AGR (Table S8 and Fig. S6), it was found that the percentage content of representative functional groups $\text{O}=\text{C}$ of AQC did not change much, indicating that AQC/AGR has good stability.

3.3. Optical properties of AQC/AGR aqueous suspensions

The optical properties such as the extinction, absorption and scattering coefficients are characteristics of every photocatalyst, affect the absorption rate of photons and are an important factor affecting the photocatalytic activity of the catalyst [40,83–86]. In this study, a six-flux radiation absorption-scattering model (SFM) was used to determine the optical properties of the synthesized samples [68]. Then the spatial distribution of the local volumetric rate of photon absorption (LVRPA) under solar irradiation was calculated in the experimental photoreactor. The use of optical parameters such as LVRPA, total rate of photon absorption (TRPA) and optical thickness (τ_{app}) allows a comprehensive analysis of the photocatalytic transformation of pollutants [40].

3.3.1. Estimation of the optical properties

The non-specific extinction coefficients (β_λ) at each concentration were calculated using Eq. (12).

$$\beta_\lambda = 2.303(-\log T_\lambda/L_{\text{cell}}) \quad (12)$$

where T_λ is the transmittance measurement, and L_{cell} is the cell path length (m). A linear regression of β_λ calculated for different concentrations of catalyst was performed by plotting the β_λ values as function of catalyst concentration (C_{cat}) to obtain the specific extinction coefficient (β_λ^* , $\text{m}^2 \text{ kg}^{-1}$).

Subsequently, for isotropic scattering, the specific absorption coef-

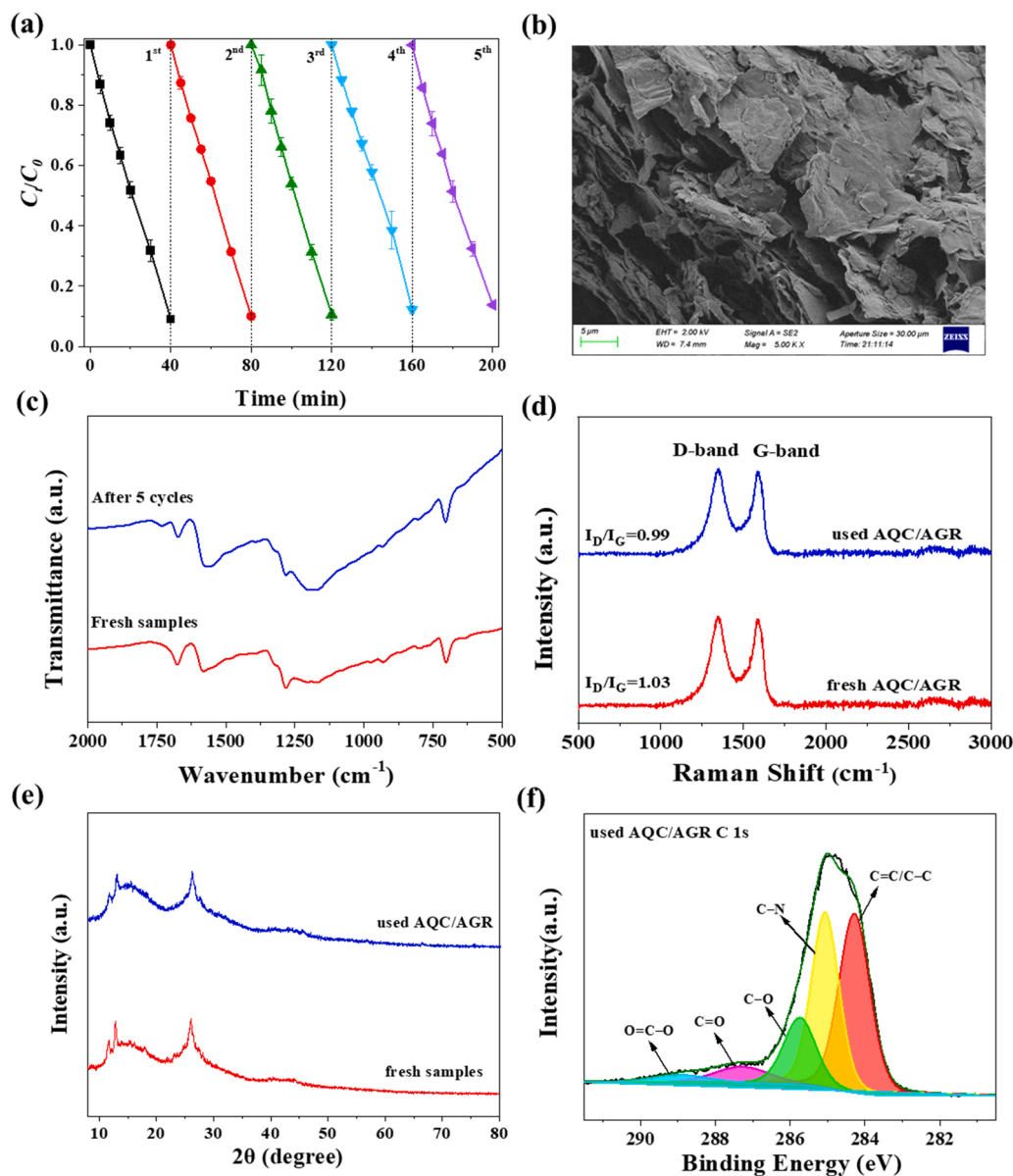


Fig. 4. (a) Five cycles of degradation of 10 mg/L TMP by 0.05 g/L AQC/AGR-1 for solar irradiation at pH 7 in the presence of 500 mM NaCl. (b) SEM image of the used AQC/AGR-1, (c) XRD patterns, (d) FTIR spectra, and (e) Raman spectra of the fresh and used AQC/AGR-1. (f) The high-resolution C 1 s XPS spectra of the used AQC/AGR-1.

efficient (κ_{λ}^*) and specific scattering coefficient (σ_{λ}^*) were obtained from Eqs. (13–16):

$$T = \frac{1}{\exp[L_{\text{cell}}(K + S)]} \quad (13)$$

$$R = \frac{S}{S + K} \left(\frac{\exp[L_{\text{cell}}(K + S)] - 1}{\exp[L_{\text{cell}}(K + S)]} \right) \quad (14)$$

where T is the diffuse transmittance measurement, R is the diffuse reflectance measurement, K and S are the optical parameters of SFM

model [68]. Similarly, the specific K values (K^*) were calculated by performing a standard linear regression for different catalyst concentrations of K values.

$$\kappa_{\lambda}^* = K^*/3 \quad (15)$$

$$\sigma_{\lambda}^* = \beta_{\lambda}^* - \kappa_{\lambda}^* \quad (16)$$

The τ_{app} and LVRPA were estimated according to Eqs. (17) and (18):

$$\text{LVRPA} = \frac{I_0}{\lambda_{\text{ocorr}} \omega_{\text{corr}} (1 - \gamma)} \times \left[(\omega_{\text{corr}} - 1 + \sqrt{1 - \omega_{\text{corr}}^2}) \exp\left(-x/\lambda_{\text{ocorr}}\right) + \gamma (\omega_{\text{corr}} - 1 - \sqrt{1 - \omega_{\text{corr}}^2}) \exp\left(x/\lambda_{\text{ocorr}}\right) \right] \quad (17)$$

$$\tau_{app} = l(S + K)\sqrt{1 - \omega_{corr}^2} \quad (18)$$

where I_0 is the solar incident radiation flux on the reactor (W m^{-2}), W_λ is the spectrum of the incident radiation ($\text{W m}^{-2} \text{ nm}^{-1}$), and the other parameters equal to:

$$\omega_{corr} = \frac{S}{S + K} \quad (19)$$

$$\lambda_{wcorr} = \frac{1}{(S + K)\sqrt{1 - \omega_{corr}^2}} \quad (20)$$

$$\gamma = \frac{1 - \sqrt{1 - \omega_{corr}^2}}{1 + \sqrt{1 - \omega_{corr}^2}} \exp(-2\tau_{app}) \quad (21)$$

$$\beta^* = \int_{\lambda_{min}}^{\lambda_{max}} \beta_\lambda^* W_\lambda d\lambda / \int_{\lambda_{min}}^{\lambda_{max}} W_\lambda d\lambda \quad (22)$$

$$\sigma^* = \int_{\lambda_{min}}^{\lambda_{max}} \sigma_\lambda^* W_\lambda d\lambda / \int_{\lambda_{min}}^{\lambda_{max}} W_\lambda d\lambda \quad (23)$$

$$\kappa^* = \int_{\lambda_{min}}^{\lambda_{max}} \kappa_\lambda^* W_\lambda d\lambda / \int_{\lambda_{min}}^{\lambda_{max}} W_\lambda d\lambda \quad (24)$$

$$p = \frac{\sigma^*}{6\beta^*} \quad (25)$$

$$K = \kappa^* \kappa^* + 3/2\sigma^* p C_{cat} / (\kappa^* + 1/2\sigma^* p) \quad (26)$$

$$S = \sigma^* \kappa^* p + 3/4\sigma^* p^2 C_{cat} / (\kappa^* + 1/2\sigma^* p) \quad (27)$$

Tables 1 and 2 depicts the calculated absorption coefficient (κ^*), extinction coefficient (β^*) and scattering coefficient (σ^*) of AQC/AGR samples. It can be seen that the effect of graphene in composites on radiation scattering is greater than that on radiation absorption [39]. The distribution of LVRPA with reactor depth for AQC/AGR-1 is shown in Fig. 5a. The irradiated boundary of the reactor has a high LVRPA value at high catalyst loading (0.2 g/L–1 g/L) and the LVRPA value decreases sharply at greater reactor depth, which is attributed to the high value of scattering albedo of the photocatalytic materials [68,86].

3.3.2. Total rate of photo absorption (TRPA)

Total rate of photon absorption (TRPA) is the overall rate of radiation absorbed in the entire reactor volume [87], and the TRPA was calculated according to the Eq. (28):

$$TRPA = \int LVRPA \cdot dx \quad (28)$$

The variation curves of TRPA/A with photocatalyst concentration are shown in Fig. 5b. The TRPA/A value increases gradually with increasing photocatalyst concentration until it plateaus. The photocatalyst dosage corresponding to TRPA/A changing less than 0.5 % variation can be considered the optimal value [86]. For AQC/AGR-1, this optimal concentration was calculated to be about 0.4 g/L, corresponding to the τ_{app} of 3.99 (Fig. 5c). In addition, the τ_{app} values of the

Table 1
Optical properties of the photocatalyst.

Photocatalyst	β^* ($\text{m}^2 \text{ kg}^{-1}$)	κ^* ($\text{m}^2 \text{ kg}^{-1}$)	σ^* ($\text{m}^2 \text{ kg}^{-1}$)
AQC/AGR-0.25	351	97	254
AQC/AGR-0.5	538	157	381
AQC/AGR-0.75	405	214	191
AQC/AGR-1	712	250	462
AQC/AGR-1.25	1068	189	879

Table 2
Optical thickness of the photocatalyst.

Concentration (g/L)	Photocatalyst				
	AQC/ AGR-0.25	AQC/ AGR-0.5	AQC/ AGR-0.75	AQC/ AGR-1	AQC/ AGR-1.25
0.025	0.11	0.17	0.18	0.25	0.29
0.05	0.22	0.35	0.35	0.50	0.57
0.075	0.33	0.52	0.53	0.75	0.86
0.1	0.44	0.70	0.71	1.00	1.14
0.125	0.55	0.87	0.88	1.25	1.43
0.15	0.66	1.04	1.06	1.50	1.71
0.2	0.89	1.39	1.42	1.99	2.28
0.3	1.33	2.09	2.12	2.99	3.42
0.4	1.77	2.78	2.83	3.99	4.56
0.5	2.22	3.48	3.54	4.99	5.70
0.75	3.32	5.21	5.31	7.48	8.55
1	4.43	6.95	7.08	9.97	11.40

obtained sample suspensions increased with increasing photocatalyst loading and is shown in Fig. 5c. The concentrations of AQC/AGR-0.25, AQC/AGR-0.5, AQC/AGR-0.75, and AQC/AGR-1.25 catalysts were about 0.88, 0.56, 0.56, and 0.34 g/L at the τ_{app} value of 3.99, respectively. To more comprehensively comparison of the photocatalytic degradation ability of different catalysts, the experiments of photocatalytic degradation of TMP were carried out at the same τ_{app} values (Fig. 5d), and AQC/AGR-1 showed the best removal rate after 40 min of solar irradiation. The results agreed with the experimental results in Fig. 3d, with only some catalysts having elevated removal rates of TMP. This is because in addition to radiation absorption, increasing the catalyst dosing will adsorb more organic pollutants.

3.3.3. Estimation of reaction kinetic parameters

Kinetic analysis of photocatalytic reactions should consider the volumetric rates of photon absorption at each location in the photoreactor space [85,88,89]. In the present work, the rate constants for TMP photocatalytic degradation were estimated, which are independent of the radiation absorbed within the photoreactor [85]. The reaction rate of AQC/AGR photocatalytic degradation of TMP can be simulated by a pseudo Langmuir-Hinshelwood (L-H) kinetic rate, as shown in Eq. (29) [88]:

$$r = \frac{k_1 K_{L-H}}{1 + K_{L-H} C_0} C_i (LVRPA)^{0.5} \quad (29)$$

where C_i is the concentration of TMP solution (kmol/m^3), C_0 is the initial concentration of TMP before irradiation, k_1 is the intrinsic kinetic constant ($\text{kmol m}^{-1.5} \text{ s}^{-1} \text{ W}^{-0.5}$), K_{L-H} is the L-H binding constant ($\text{m}^3 \text{ kmol}^{-1}$).

The L-H parameters of the kinetic model were obtained by a nonlinear least-squares optimization procedure that resulted in the best fit of the experimental data [88], as shown in Table 3, which is consistent with the experimental results in Table S3. These reaction kinetic parameters, which are independent of the irradiation conditions and reactor geometry in the reactor, are more suitable for the design and evaluation of photocatalytic reactors [85,88].

3.4. Identification of reactive species

Radical quenching experiments were used to identify and investigate the contributions of specific reactive species during the photoactivation process. The reaction rate constants between $\cdot\text{OH}$, $\text{Cl}\cdot$, and $\text{Cl}_2\cdot^-$ and the quencher are supplemented in Text S3. Herein, sorbic alcohol (SA), chloroform (CF), and L-histidine (LH) were used to selectively eliminate excited AQC/AGR, $\text{O}_2^{\cdot-}$, and $^1\text{O}_2$. After the addition of SA, no significant TMP removal was observed (Fig. 6a), implying that the light-excited photoactive component (AQC/AGR*) initiated the degradation of TMP. The decrease in TMP removal rate in the presence of CF (1 mM) or

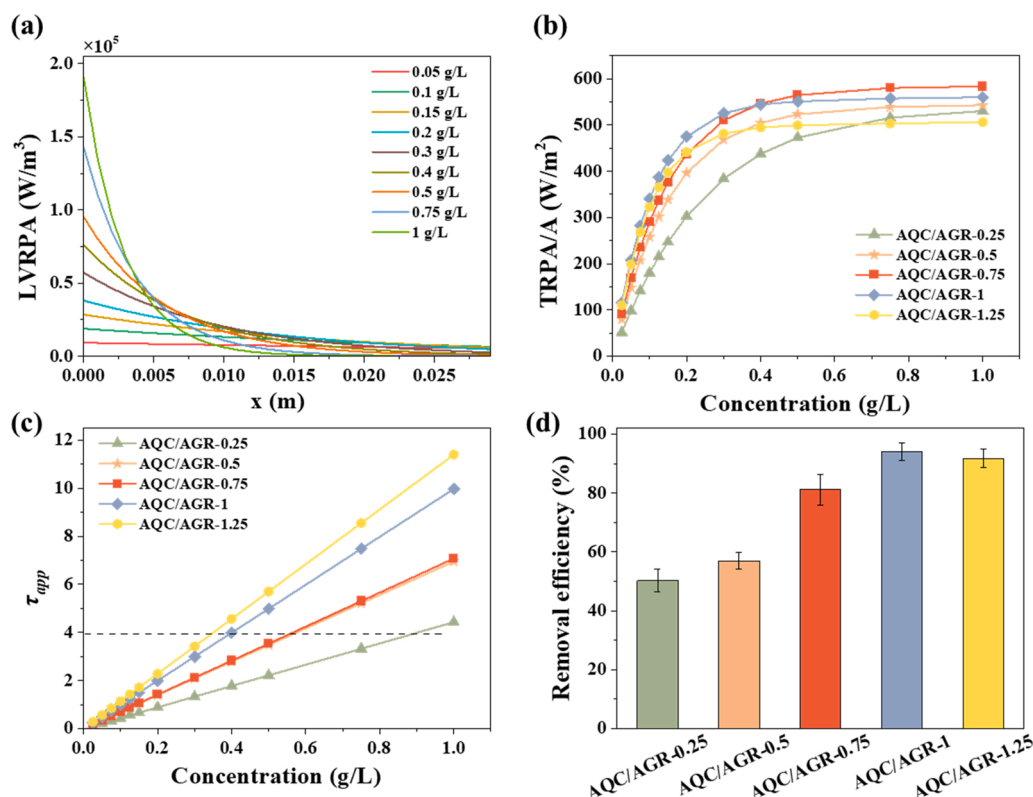


Fig. 5. (a) The distribution of LVRPA of AQC/AGR-1. (b) Photocatalyst concentration dependent TRPA/A profile. (c) Photocatalyst concentration dependent τ_{app} profile. (d) Photocatalytic degradation experiments at equal optical thickness by AQC/AGR samples with different mass ratios under solar irradiation.

Table 3

Reaction rate constants (Eq. 29) of TMP photocatalytic degradation by the AQC/AGR samples.

Photocatalyst	$k \times 10^{-10}$ (kmol m ^{-1.5} s ⁻¹ W ^{-0.5})	$K_{L-H} \times 10^4$ (m ³ kmol ⁻¹)
AQC/AGR-0.25	0.489	5.79
AQC/AGR-0.5	0.906	4.29
AQC/AGR-0.75	4.88	3.06
AQC/AGR-1	9.46	4.01
AQC/AGR-1.25	5.19	3.55

L-ascorbic acid (L-AA) demonstrated the crucial role of $\cdot\text{O}_2^-$ (Fig. S7a) [90]. Similarly, the variation in the proportion of transformed NBT indicated that $\text{O}_2^{\cdot-}$ was formed in the AQC/AGR photocatalytic system (Fig. 6b). Furthermore, Continuous sparging of N₂ during the photocatalytic reaction to verify the role of $\text{O}_2^{\cdot-}$. As shown in Fig. S7b, the degradation rate of TMP was 99 % in 40 min under air purging conditions, while the degradation rate of TMP was 76 % under N₂ purging conditions. The results indicated that the purging N₂ significantly inhibited the degradation of TMP while air purging promoted the degradation of TMP. This is because the increased dissolved oxygen concentration accelerated the rate of ROS and RCS production by the photocatalyst, which confirms the critical role of O₂ in capturing electrons from the AQC/AGR radical anion and returning AQC/AGR to the ground state. The addition of *tert*-butyl alcohol (TBA, 10 mM) slightly suppressed TMP degradation. In contrast, after adding 250 mM isopropyl alcohol (IPA), the degradation of TMP was diminished to 55.50 %, suggesting that Cl^\cdot played a minor role because at high chloride ion concentration, Cl^\cdot was converted to $\text{Cl}_2^{\cdot-}$, which was the main contributor to the photocatalytic process (Fig. 6a and Text S3). When higher concentrations of TBA are added to the reaction system, the reaction is gradually inhibited, so $\cdot\text{OH}$ radicals also play a non-negligible role in the reaction system (Fig. S7c). Although LH exhibited significant inhibition

of TMP degradation, the role of $^1\text{O}_2$ was found to be uninvolved in the photocatalytic reaction, with the results shown in Fig. S7d-f and Text S7. Furthermore, with the addition of EDTA (1 mM) as an h^+ scavenger, the removal efficiency of AQC/AGR did not change much, indicating that h^+ was not the key reactive species during the photoinduced process (Fig. S7g). These findings demonstrate that the reactive species are more likely produced in the electron transfer process between AQC/AGR* and Cl^- rather than through the energy transfer process to generate $^1\text{O}_2$.

5,5-dimethyl-1-pyrrolidine-N-oxide (DMPO) has been frequently applied to trap $\cdot\text{OH}$ and $\text{O}_2^{\cdot-}$ in spin trapping EPR measurements. Virtually no apparent EPR signals were found under dark conditions. A DMPO- $\text{O}_2^{\cdot-}$ signal was detected in the presence of AQC/AGR-1 under solar irradiation (Fig. 6c), and the signal intensity enhanced with the increase in the concentration of Cl^- (Fig. 6e), confirming that the co-existence of Cl^- promoted the photoinduced-formation of $\text{O}_2^{\cdot-}$. Additionally, the unique signal has been reported to be of $\text{O}_2^{\cdot-}$ [91,92]. As shown in Fig. 6d, upon solar irradiation, AQC/AGR-1 exhibited four characteristic signals of $\cdot\text{OH}$ with an intensity ratio of 1:2:2:1, while the peaks intensified with the extension of irradiation time. In addition, EPR tests of AQC/AGR-1 with PBN were performed, and it is hypothesized that $\text{Cl}_2^{\cdot-}$ were generated during AQC/AGR photoactivation of Cl^- (Fig. 6f and Text S7), and the signal intensity was enhanced with the increase in the concentration of Cl^- (Fig. S7h). Unexpectedly, a triplet of doublets in the presence of AQC/AGR-1 was observed in the aqueous solution of PBN aqueous solution containing NaCl, which is the characteristic feature of the hydroxy adduct of PBN (Fig. S7i) [93]. This indicated that excess $\text{Cl}_2^{\cdot-}$ could react with OH^- to form OH^\cdot according to Eqs. (S14) and (S15). Semiquinone-like radical signals with a g factor of around 2.0030 appeared in the AQC/AGR system in the presence of NaCl under solar irradiation (Fig. S7g), demonstrating the transformation between the semiquinone radical and AQC [94]. These results verify that producing of various radicals during AQC/AGR photocatalytic activation of Cl^- is crucial to the degradation of PPCPs.

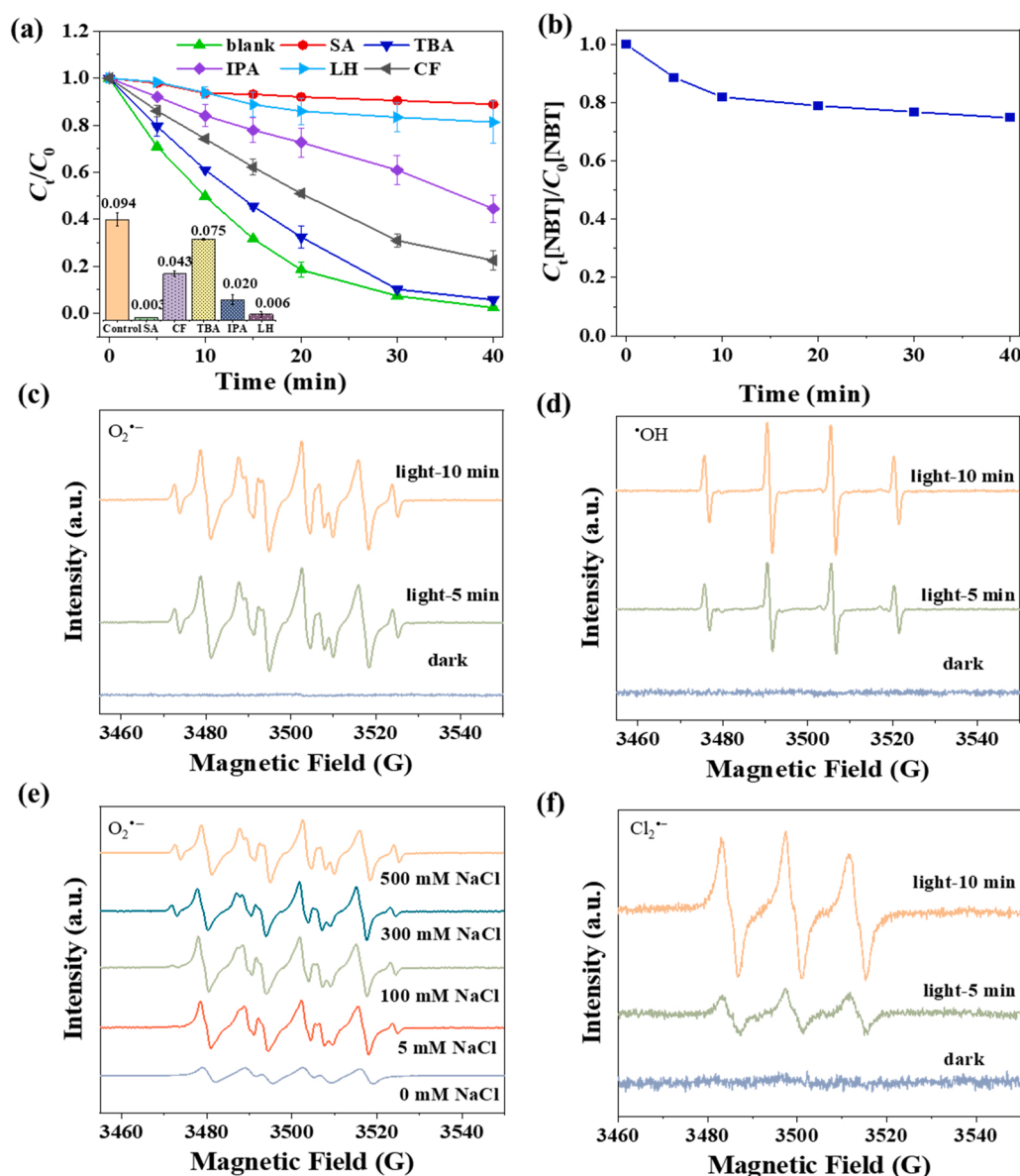


Fig. 6. (a) Effect of radical scavengers on TMP degradation ($[TMP] = 10 \text{ mg/L}$, $[AQC/AGR] = 50 \text{ mg/L}$, $[NaCl] = 500 \text{ mM}$, initial $pH = 7.0$, and error bars indicate one standard deviation). (b) Photodegradation NBT over AQC/AGR-1 under solar irradiation. EPR spectra using DMPO for (c) $O_2^{\bullet-}$ and (d) $\bullet OH$ with the catalyst of AQC/AGR-1 in the presence of NaCl (500 mM) under solar irradiation. (e) EPR spectra of the DMPO- $O_2^{\bullet-}$ at various NaCl concentration under solar light irradiation. (f) EPR spectra in the PBN benzene aqueous under solar irradiation (with a small amount of water added by sonication to ensure the dispersion of NaCl).

3.5. TMP degradation pathways and toxicity assessment

As we discussed, ROS and $Cl_2^{\bullet-}$ are the predominant reactive radicals in the AQC/AGR photocatalytic activation of Cl^- system. Moreover, RCS can react with PPCPs through multiple reaction pathways, such as single electron transfer (SET), hydrogen abstraction, and Cl addition pathways [61], wherein the SET pathway has a higher reaction rate constant than the other two pathways [95]. The reactive sites of TMP were explored through DFT calculations. The distributions of electrostatic potential (ESP) of TMP were calculated and graphically represented in red (negative regions) and blue (positive regions) colors for electrophilic and nucleophilic reactivities, respectively (Fig. 7a). These areas with negative ESP regions around the pyrimidine ring and methoxy group were more prone to electrophilic attack by $\bullet OH$ and $Cl_2^{\bullet-}$, with consequent hydroxylation, demethylation and carbonylation [96]. As shown in Fig. S8, TMP's frontier molecular orbital distribution was mainly concentrated in the diaminopyrimidine ring, benzene ring, and oxygen atoms of the trimethoxy group, indicating that these regions could potentially be the most active.

The Fukui function is a common way to predict the reactive sites of TMP, which are most susceptible to attacks by reactive species. The

contour surfaces of Fukui function values of f^0 and f^- are shown in Fig. 7c. The relatively high f^0 values in the TMP molecule were located at C1, N7, C2, C3, and N6 atoms (Table S9), indicating that the pyrimidine ring was the most vulnerable to be attacked by radicals. Furthermore, the pyrimidine ring with larger f^+ and f^0 values are susceptible to getting electron and being attacked by $O_2^{\bullet-}$, and these sites with high f^0 values were also likely attacked by $\bullet OH$ radicals, leading to the cleavage of the pyrimidine ring and the production of hydroxylation and carbonylation products (Fig. S8c and Table S9) [97,98]. The high f^- values were around C2, N7, N11, and N8 atoms, implying that these atoms with higher nucleophilicity were more accessible to electrophilic $\bullet OH$ and $Cl_2^{\bullet-}$. Moreover, C2 with the highest f^- (0.092518) could be easily attacked by radicals through an electron-transfer reaction and undergoes a deprotonation process to form carbon (C14)-centered radical [99]. Subsequently, α -hydroxytrimethoprim and α -keto-trimethoprim were formed because of functionalization at the C14 atom.

HPLC/Q-TOF-MS further identified the intermediate products formed during the degradation of TMP. The total ion chromatogram (TIC) and related mass spectra of the major degradation products of TMP at different retention times are displayed in Fig. S9. The structure, molecular formula, and m/z of the degradation products of TMP are listed

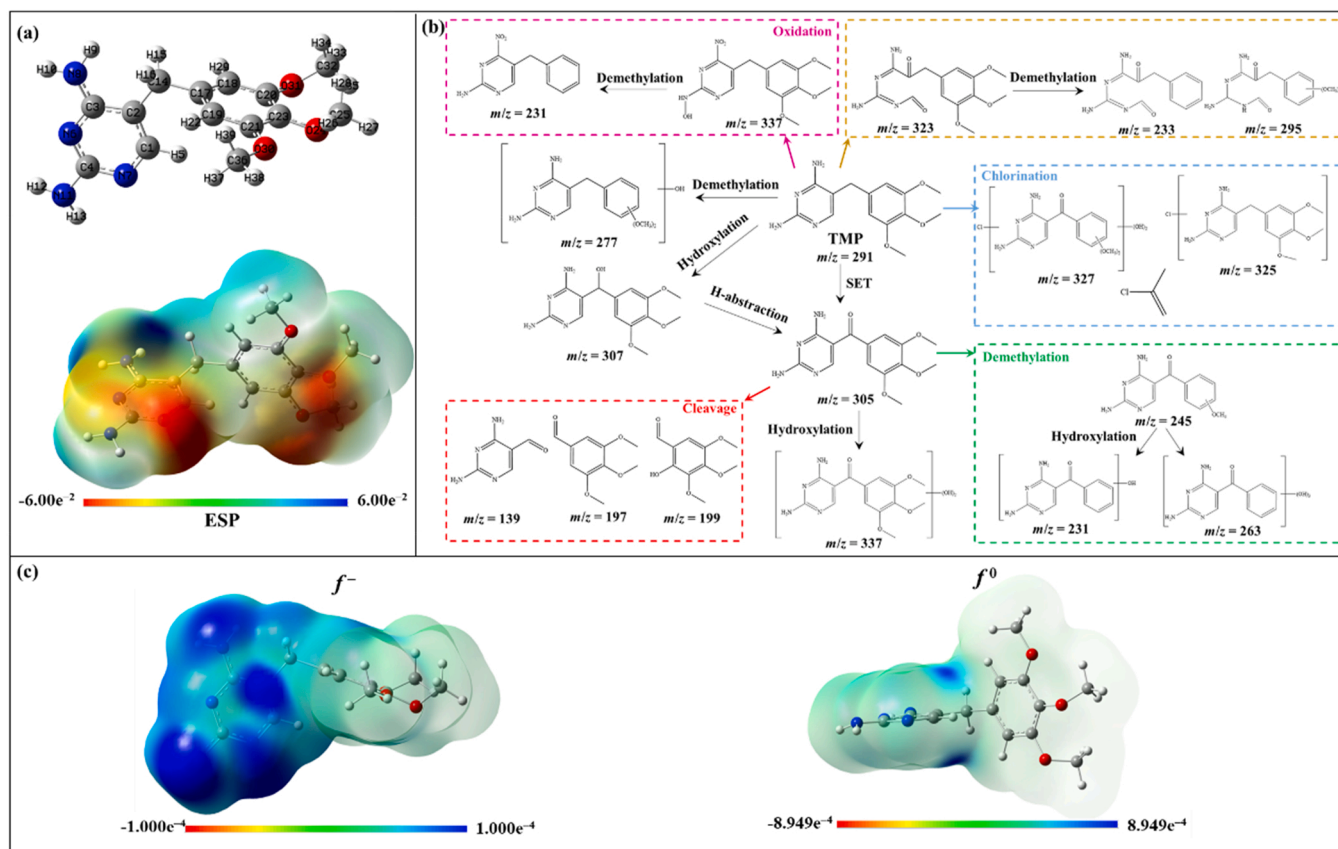


Fig. 7. (a) Optimized structure of TMP and the numbering system (gray: carbon; red: oxygen; blue: nitrogen; white: hydrogen); Electrostatic potential (ESP) distributions of TMP. (b) The proposed degradation pathway of TMP. (c) The contour surfaces of Fukui function for electrophilic attack (f^-) and radical attack (f^0) on TMP.

in Table S10. The proposed degradation pathway of TMP is depicted in Fig. 7b. $\text{Cl}_2^{\bullet-}$ can react with the electron-donating group on TMP through the electron transfer process with a rate constant of $(1.88 \pm 0.23) \times 10^9 \text{ M}^{-1} \text{ s}^{-1}$ [61]. The general degradation mechanisms of TMP (m/z 291, $\text{C}_{14}\text{H}_{19}\text{N}_4\text{O}_3$) involved various reactions including hydroxylation, carbonylation, demethylation, and Cl-substitution reaction. The product P277 (m/z 277) was formed through the demethylation of TMP. The hydroxylated TMP (P307) may exist in many isomeric structures and the diaminopyrimidine ring, benzene ring, and bridging methylene group. Furthermore, P307 can further be oxidized to form P305 ($\text{C}_{14}\text{H}_{17}\text{N}_4\text{O}_4$), a significant intermediate and has also been observed in several other AOPs [97,99]. The P305 intermediate can be transformed into P337, P245, P231, and P263 through hydroxylation and demethylation. The broken C1=C2 double bond by radicals resulted in the cleavage of the pyrimidine ring and yielded P323 (C1 and C2 with relatively high f^0 and f^- values). In addition, P295 and P233 were generated after the demethylation reaction of P323. The cleavage of P305 resulted in the formation of P197, P139, and P199. Regrettably, several chlorine-containing intermediates were identified in the AQC/AGR photocatalytic system, where P327 ($\text{C}_{13}\text{H}_{16}\text{N}_4\text{O}_4\text{Cl}$) and P325 ($\text{C}_{14}\text{H}_{18}\text{N}_4\text{O}_3\text{Cl}$) corresponded to monochlorinated TMP. It has been reported that $\text{Cl}_2^{\bullet-}$ reacts with pollutants bearing electron-rich moieties (such as SDZ, domoic acid, thioethers, and gemfibrozil) through oxidation rather than adding chlorine atoms [69,95,100,101]. Therefore, the chlorinated byproducts (P327 and P325) were probably derived from the substitution of the Cl atom by free chlorine. Additionally, $\text{O}_2^{\bullet-}$ has strong nucleophilicity and reducing power ($E^0(\text{O}_2/\text{O}_2^{\bullet-}) = -0.33 \text{ V}$) [102], which is expected to promote the reductive dechlorination of chlorinated TMP. Moreover, when chlorinated disinfection byproducts (DBPs) were analyzed by GC-MS, common

chlorinated products such as chloroform, chloral hydrate, dichloroacetonitrile, and trichloronitromethane were absent in the degraded TMP solution [71], while the chlorinated product detected was 2-chloropropene ($\text{C}_3\text{H}_5\text{Cl}$). It means that the reaction between $\text{Cl}_2^{\bullet-}$ and TMP is dominated by oxidation rather than chlorine addition [100]. It may also be related to the nucleophilicity of $\text{O}_2^{\bullet-}$, which can react with chlorinated products for dechlorination to favor the subsequent degradation [102,103].

Intermediates from photocatalytic processes may exhibit toxicity, jeopardizing the environment and human health [8]. Therefore, the toxicity of TMP and TMP-derived degradation products was analyzed using T.E.S.T. Most products showed higher LC_{50} for fathead minnow (*Pimephales promelas*) (96 h) and *Daphnia magna* (48 h) (Table S11), suggesting a decreased ecotoxicity to fathead minnow and *Daphnia magna* after the catalytic treatment. Nevertheless, the ecotoxicity of P263, P327, and P325 increased. Most byproducts' bioaccumulation factor and mutagenicity of were lower than TMP's (Table S11). Unfortunately, the intermediates P263 and P127 had positive mutagenicity, which was probably due to the reason that the resulting phenol derivatives were more acutely toxic. In general, the toxicity of TMP diminished, and it transformed into less-toxic substances by the AQC/AGR/ Cl^- photocatalytic system.

3.6. Optical absorption and electrochemistry analysis

AQC displayed a broad absorption band in the UV and visible light regions, and exhibited an absorption maximum at 483 nm (Fig. 8a). AQC/AGR-1 absorbed strongly in the whole range of visible light compared to that of AGR. From the Tauc approach (Eq. 1), E_g for AQC and AQC/AGR-1 are determined to be 2.65 and 2.42 eV, respectively.

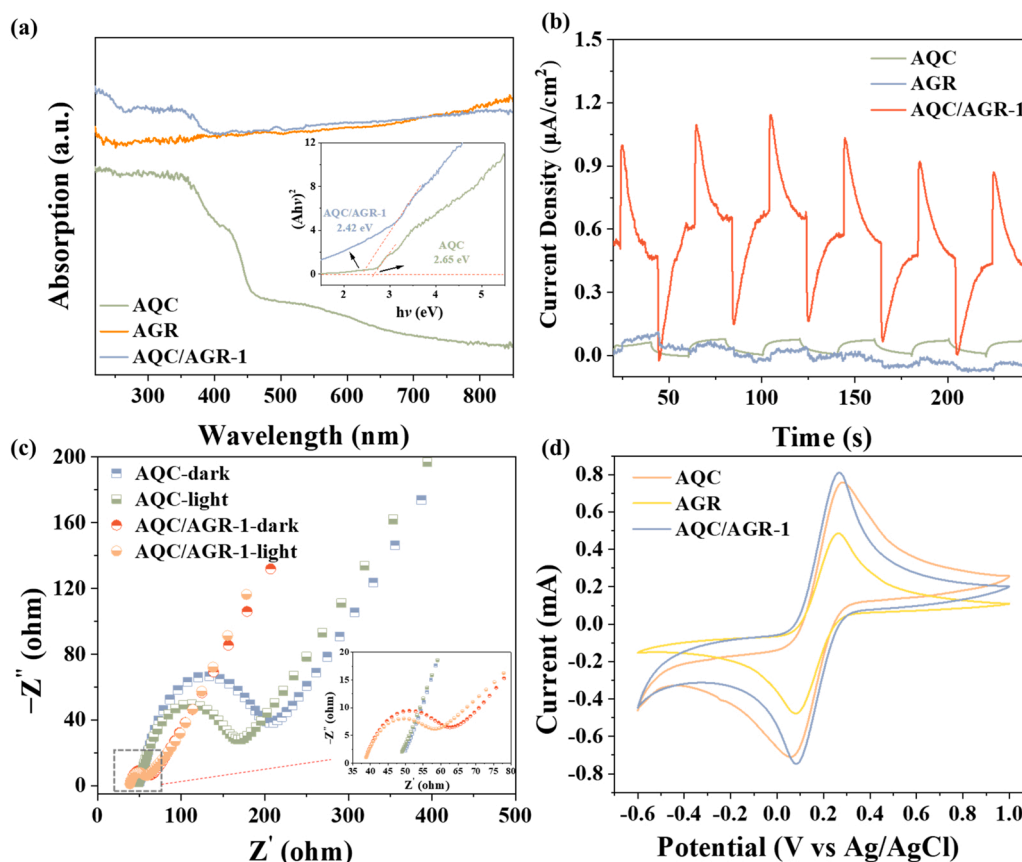


Fig. 8. (a) UV-vis DRS spectra of AQC, AGR and AQC/AGR-1 with insets showing the band gaps of AGR and AQC. (b) Photocurrent spectra with several intermittent on-off cycles. (c) EIS Nyquist plots. (d) CV curves for the samples collected at 100 mV/s from -0.6 V to 1 V.

The Mott–Schottky (M-S) plot of AQC/AGR-1 exhibited a positive slope, indicating its n-type semiconductor behavior (Fig. S10a). AQC/AGR-1's flat-band potential is -0.83 V (vs. Ag/AgCl). Accordingly, the normal hydrogen electrode (NHE) potential of AQC/AGR-1 was -0.63 V (vs. NHE), based on the $E_{\text{NHE}} = E_{\text{Ag/AgCl}} + 0.197$ V. The conduction band (CB) bottom position was determined to be -0.63 V for AQC/AGR-1. The photogenerated electrons can react with an oxygen molecule to produce $\text{O}_2^{\bullet -}$. According to the equation " $E_{\text{VB}} = E_{\text{CB}} + E_{\text{g}}$ ", the valence band edge of AQC/AGR-1 is 1.79 V (vs. NHE).

The photoexcited carrier separation and transfer were evaluated by measuring the transient photocurrent response with several intermittent on-off cycles under simulated solar irradiation. As delineated in Fig. 8b, the transient photocurrent density of AQC/AGR is higher than that of AQC, indicating that graphene is indispensable in facilitating the mobility of the photogenerated carrier and interfacial transport of electrons, thus prolonging the lifetime of the generated electron. Besides, non-sensitized AGR does not show an obvious photocurrent response after illumination, in agreement with its negligible photocatalytic activity mentioned soon [67].

Electrochemical impedance spectroscopy (EIS) was employed to investigate the interfacial electron transfer of the as-prepared samples. The semicircle radius of AQC/AGR-1 is significantly smaller than AQC in the Nyquist plot. It indicates a lower interfacial charge transfer impedance of AQC/AGR-1. It suggests that the electron transport of AQC/AGR-1 can be accelerated by graphene due to the strong interface connection between graphene and AQC (Fig. 8c). Moreover, the charge transfer resistance of AQC and AQC/AGR-1 lowered after solar illumination, demonstrating that both AQC/AGR-1 and AQC could be excited independently under sunlight [104]. Surprisingly, introducing of non-conductive AQC into the composite did not affect the high electron conductivity of the graphene noticeably (Fig. S10b), indicating that the

sp^2 conjugated structure of graphene-modified with AQC is not damaged [25].

As shown in Fig. 8d, all three samples showed characteristic redox peaks in cyclic voltammetry (CV) curves. The pronounced CV curve of AGR is attributed to oxygen-containing functional groups present in AGR [25]. The stable CV curve of AQC exhibited a cathodic reduction peak centered at 0.056 V vs. Ag/AgCl and an anodic oxidation peak at 0.284 V due to the redox shuttle properties of AQC containing carbonyl moieties (quinone to hydroquinone). AQC/AGR-1 displayed an enhanced redox couple compared to bare AQC and AGR, demonstrating a higher electric capacity of AQC/AGR-1 [25] and enhanced electron transfer of the redox pair due to the high conductivity of graphene and electrochemical activity of AQC. The separation-recombination of photogenerated carriers of the samples was investigated by photoluminescence (PL) spectra. The PL intensity of AQC/AGR-1 is much weaker than AQC (Fig. S10c), indicating the energetic photo-excited charge separation of composites by combining graphene with AQC. Graphene could shift the HOMO of AQC to lower energies via $\pi - \pi^*$ or charge-transfer interactions [105].

3.7. Theoretical insights into the mechanism of photoactivation of Cl^-

Spin density differences can be qualitatively evaluated by considering Mulliken spin populations using Gaussian 16 [106]. In the photoexcited triplet state of AQC, the spin populations on C7 and O23 atoms were 0.32 and 0.99 , respectively (Fig. S11 and Table S12). When Cl^- was encountered, the spin population was concentrated exclusively on O23 (0.66) and Cl28 (0.48), indicating that the unpaired electrons may reside on the oxygen atom for the carbonyl of AQC and the chloride ion upon photoexcitation of AQC. This indicates that intermolecular charge-transfer excitation occurred between the excited AQC and the

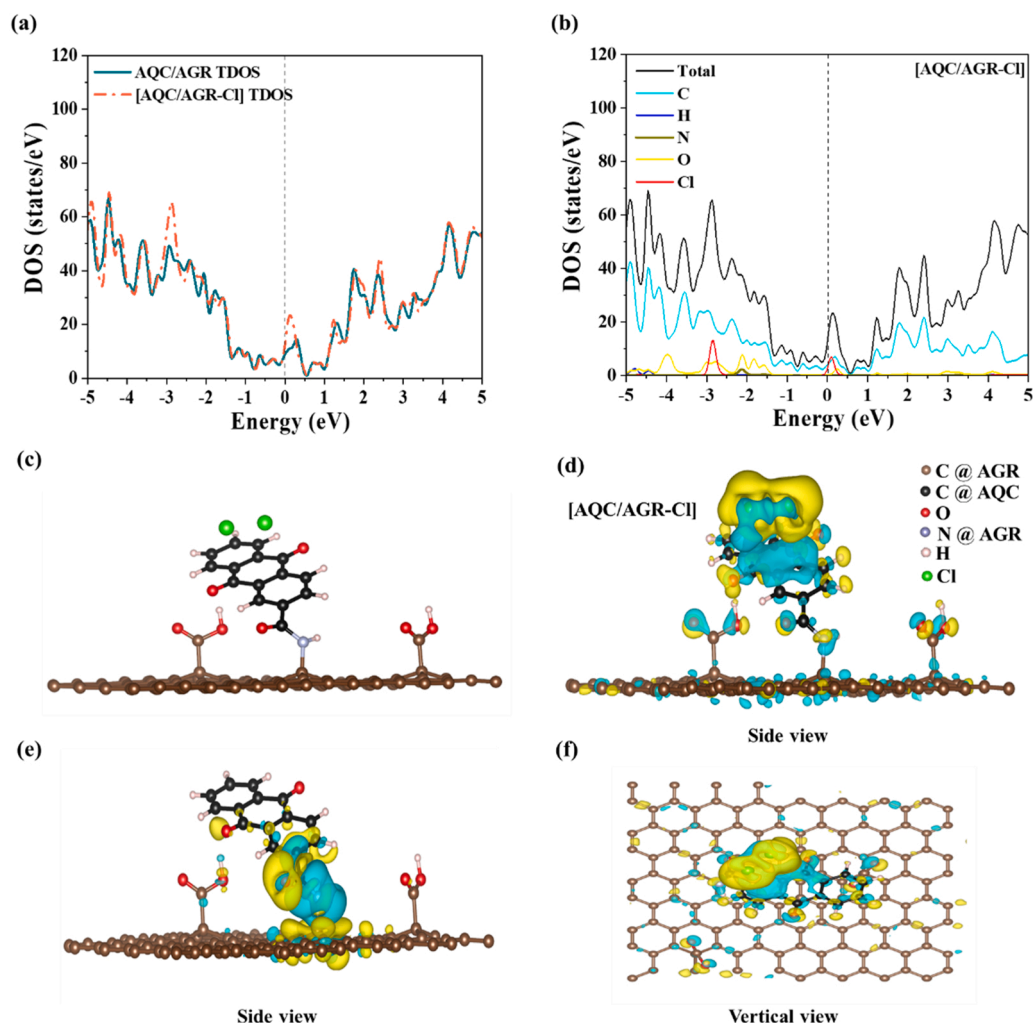


Fig. 9. (a) DOS for AQC/AGR and [AQC/AGR-Cl]. (b) PDOS for [AQC/AGR-Cl]. (c) The optimized geometries of chloride ions adsorbed on AQC/AGR ([AQC/AGR-Cl]). Charge density difference of (d) [AQC/AGR-Cl] and (e) AQC/AGR with side view. (f) Charge density difference of [AQC/AGR-Cl] with vertical view. (Yellow and cyan isosurfaces represent electron accumulation and electron depletion, respectively).

Cl^- , wherein Cl^- was converted into chlorine radicals.

Moreover, DFT calculations were conducted to probe the electronic structure of AQC/AGR [25], and the structures of AQC/AGR and AQC/AGR coupled with Cl ([AQC/AGR-Cl]) are shown in Figs. S12 and 9c. The density of states (DOS) near the Fermi level of [AQC/AGR-Cl] was higher than that of AQC/AGR and slightly shifted to the downward energy region, where the increased electronic state from adsorbed Cl^- was merged with bands above the Fermi level (Figs. 9a and S13). According to the partial density of states (PDOS) for "Cl" (Fig. 9b), the Cl-3p orbital participates in the composition of CB, wherein the empty bands would provide more capacities to store charges, which is beneficial to their fast charge transfer reactions [25,46]. The calculated work function of AQC/AGR was 4.41 eV (Fig. S14), while the [AQC/AGR-Cl] system showed a slightly increased work function (4.51 eV). This is owing to the Cl atoms' high electronegativity and because graphene is a conductive material that acts as a conductive bridge to facilitate the electron transfer between chloride ions and AQC/AGR [107]. These results suggest strong hybridization interaction (Cl, C, and O atoms) and electronic modulation of AQC/AGR and Cl^- .

Bader charge analysis revealed that 0.22 |e| was transferred from AQC to AGR through chemical bonding, possibly due to the interfacial polarization electric field promotion at the interface of AQC and graphene (Table S13). In the case of Cl^- adsorbed on the surface of AQC/AGR, the carbonyl O on AQC and amino N on AGR catch electrons, and

about 0.31 |e| transferred from AQC to AGR. The two chloride ions experienced an electron depletion (0.10 |e|) and an electron accumulation (0.13 |e|) process, which improved the electron transfer within the interface of the hybrid structure (in the formation of charge-transfer exciplex). It led to the cleavage of exciplex [(AQC/AGR-Cl-Cl) $^{*2-}$] that generated Cl_2^{*2-} . The charge density distributions were concentrated at the interface of AQC and AGR through the intimate linkage channels (Fig. 9e), promoting the interfacial electron transfer and providing the active site where the reaction occurs. After being in contact with Cl^- , the stable [AQC/AGR-Cl] configuration showed a significant charge redistribution, while the transfer of charge density difference mainly occurred at the interface of AQC/AGR and Cl^- (Fig. 9d and f). Both AQC and graphene participated in the charge transfer process, and there was significant interaction in the interlayer between Cl^- and AQC/AGR, where strong chemisorption may have occurred. More negative and positive centers near chloride ions could lead to an effective electron transfer of Cl^- to AQC/AGR.

Based on the results of experiments and theoretical calculations, a plausible mechanism for the removal of organic contaminants from Cl^- -containing waters of AQC/AGR photocatalytic activation of Cl^- is delineated in Fig. 10. Under solar irradiation, AQC can form the singlet excited state ($^1\text{AQC}^*$) from the ground state, which in turn produces the triplet excited state ($^3\text{AQC}^*$) via an intersystem crossing (ISC). AQC has a tight interfacial connection with graphene, which facilitates rapid

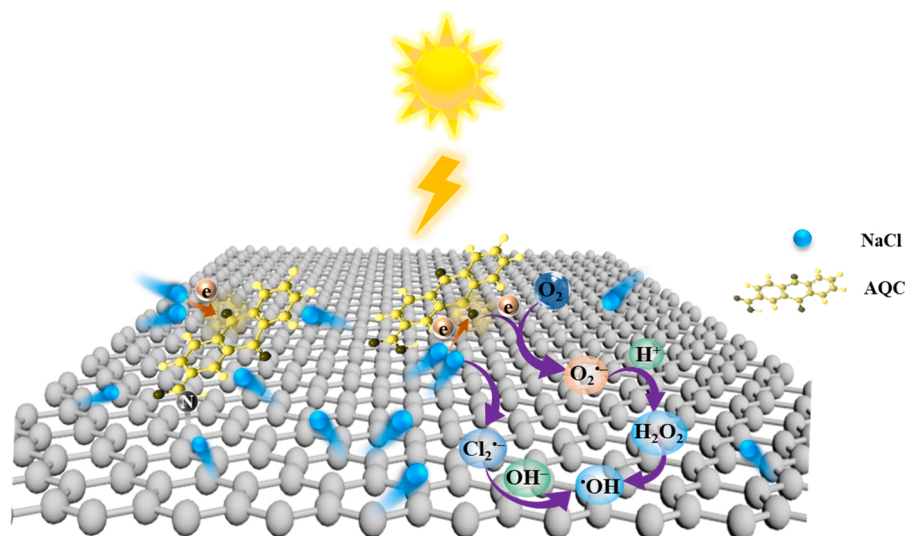


Fig. 10. A schematic diagram of AQC/AGR photocatalytic activation of chloride ions and production of reactive species under simulated solar irradiation.

electron transfer at the active interface. After the bonding of light-driven AQC/AGR with chloride ions, electrons generated from the charge-transfer exciplexes were transferred from chloride ions to AQC/AGR to generate $\text{Cl}_2^{\bullet-}$, and while the accumulated electrons of AQC/AGR were transferred through the graphene surface to oxygen to generate $\text{O}_2^{\bullet-}$, which accelerates the production of ROS. $\text{Cl}_2^{\bullet-}$ can react with OH^- to form $\bullet\text{OH}$; meanwhile $\bullet\text{OH}$ could be generated by the chain reactions of $\text{O}_2^{\bullet-}$ [108]. Moreover, AGR performed as an interfacial transmission channel for substrates (such as chloride ions and PPCPs) and electrons. Besides, it can increase the number of active sites, further enhancing the opportunity for AQC to come into contact with chloride ions. The enhanced electron delocalization effect induced by the strong coupling of AQC with AGR strengthened the interfacial carrier-separation capacity between AQC/AGR and chloride ions.

4. Conclusions

Herein, an AQ-modified graphene-based photocatalyst, AQC/AGR, was successfully designed and constructed via a mild two-step preparation method. Integrating AQ onto graphene conveniently modulated photoinduced carrier separation and formed interfacial charge transport space. Moreover, in a solar-radiation-driven fashion, AQC/AGR efficiently removed PPCPs from Cl^- -containing water with excellent reusability and stability. The experimental analysis and DFT calculations revealed the processes involved in migrating photogenerated carriers and generating active species; $\text{O}_2^{\bullet-}$, $\bullet\text{OH}$ and $\text{Cl}_2^{\bullet-}$ were the dominant radicals participating in TMP degradation (involving hydroxylation, carbonylation, and demethylation reactions) in the process of activation of Cl^- by light-excited AQC/AGR. This metal-free carbon-based nanocatalyst provides a new and promising direction for designing catalysts for in situ photoactivation of Cl^- in brine containing a high concentration of Cl^- , facilitating the development of solar-powered PPCPs-degradation systems in the future.

CRedit authorship contribution statement

Cheng-Xin Chen: Conceptualization, Methodology, Investigation, Writing – original draft, Software, Data curation. **Shan-Shan Yang:** Conceptualization, Supervision, Validation, Writing – review & editing. **Jie Ding:** Supervision, Validation, Writing – review & editing. **Lan Ding:** Software, Resources. **Rui Wu:** Validation, Investigation. **Lu-Ming Liu:** Supervision, Validation. **Ji-Wei Pang:** Methodology, Formal analysis. **Lei He:** Conceptualization, Methodology. **Jun-Qiu Jiang:**

Software, Formal analysis. **Nan-Qi Ren:** Project administration, Supervision.

Declaration of Competing Interest

The authors declare that they have no known competing financial interests or personal relationships that could have appeared to influence the work reported in this paper.

Data availability

Data will be made available on request.

Acknowledgements

The authors gratefully acknowledge financial support from the National Natural Science Foundation of China (Grant No. 52170073), the National Engineering Research Center for Bioenergy (Harbin Institute of Technology, Grant No. 2021A001), and the Open Project of State Key Laboratory of Urban Water Resource and Environment (Harbin Institute of Technology) (Grant No. HCK202112). We gratefully thank the contribution of the algorithm model and tool support by the artificial intelligence department of CECEP Talroad Technology Co., Ltd. We gratefully acknowledge the support of Heilongjiang Province Touyan Team.

Appendix A. Supporting information

Supplementary data associated with this article can be found in the online version at [doi:10.1016/j.apcatb.2023.122823](https://doi.org/10.1016/j.apcatb.2023.122823).

References

- [1] H. Wang, Y. Wu, M. Feng, W. Tu, T. Xiao, T. Xiong, H. Ang, X. Yuan, J.W. Chew, Visible-light-driven removal of tetracycline antibiotics and reclamation of hydrogen energy from natural water matrices and wastewater by polymeric carbon nitride foam, *Water Res.* 144 (2018) 215–225.
- [2] L. He, C. Yang, J. Ding, M.Y. Lu, C.X. Chen, G.Y. Wang, J.Q. Jiang, L. Ding, G. S. Liu, N.Q. Ren, S.S. Yang, Fe, N-doped carbonaceous catalyst activating periodate for micropollutant removal: Significant role of electron transfer, *Appl. Catal. B Environ.* 303 (2022), 120880.
- [3] G. Zhao, J. Ding, F. Zhou, Q. Zhao, K. Wang, X. Chen, Q. Gao, Insight into a novel microwave-assisted W doped BiVO_4 self-assembled sphere with rich oxygen vacancies oriented on rGO ($\text{W-BiVO}_{4-x}/\text{rGO}$) photocatalyst for efficient contaminants removal, *Sep. Purif. Technol.* 277 (2021), 119610.
- [4] C. Chen, S. Yang, J. Ding, G. Wang, L. Zhong, S. Zhao, Y. Zang, J. Jiang, L. Ding, Y. Zhao, L. Liu, N. Ren, Non-covalent self-assembly synthesis of AQ2S@rGO

- nanocomposite for the degradation of sulfadiazine under solar irradiation: the indispensable effect of chloride, *Appl. Catal. B Environ.* 298 (2021), 120495.
- [5] Y. Yu, D. Chen, W. Xu, J. Fang, J. Sun, Z. Liu, Y. Chen, Y. Liang, Z. Fang, Synergistic adsorption-photocatalytic degradation of different antibiotics in seawater by a porous g-C₃N₄/calcined-LDH and its application in synthetic mariculture wastewater, *J. Hazard. Mater.* 416 (2021), 126183.
 - [6] H. Wang, Z. Han, Y. Zhou, X. Liu, D. Zeng, W. Wang, D. Sarker, L. Zhang, W. Wang, Efficient photocatalytic chlorine production on bismuth oxychloride in chloride solution, *Appl. Catal. B Environ.* 297 (2021), 120436.
 - [7] A. Katz, A. McDonagh, L. Tijting, H.K. Shon, Fouling and inactivation of titanium dioxide-based photocatalytic systems, *Crit. Rev. Environ. Sci. Technol.* 45 (2015) 1880–1915.
 - [8] R. Bruninghoff, A.K. van Duijne, L. Braakhuis, P. Saha, A.W. Jeremiasse, B. Mei, G. Mul, Comparative analysis of photocatalytic and electrochemical degradation of 4-ethylphenol in saline conditions, *Environ. Sci. Technol.* 53 (2019) 8725–8735.
 - [9] A. Sharma, N. Liu, Q.S. Ma, H.Y. Zheng, N. Kawazoe, G.P. Chen, Y.N. Yang, PEG assisted P/Ag/Ag₂O/Ag₃PO₄/TiO₂ photocatalyst with enhanced elimination of emerging organic pollutants in salinity condition under solar light illumination, *Chem. Eng. J.* 385 (2020), 123765.
 - [10] Y.T. Yu, W.C. Xu, J.Z. Fang, D.D. Chen, T. Pan, W.H. Feng, Y. Liang, Z.Q. Fang, Soft-template assisted construction of superstructure TiO₂/SiO₂/g-C₃N₄ hybrid as efficient visible-light photocatalysts to degrade berberine in seawater via an adsorption-photocatalysis synergy and mechanism insight, *Appl. Catal. B Environ.* 268 (2020), 118751.
 - [11] Z. Wang, Z. Liu, J. Huang, Y. Chen, R. Su, J. He, G. Lv, B. Gao, W. Zhou, Y. Wang, Z. Wang, Q. Li, Zr₆O₈-porphyrinic MOFs as promising catalysts for the boosting photocatalytic degradation of contaminants in high salinity wastewater, *Chem. Eng. J.* 440 (2022), 135883.
 - [12] G. Minsu, D.-Y. Lee, J. Mun, D. Kim, H.-i Cho, B. Kim, W. Kim, G. Lee, B.-S. Kim, H.-i Kim, Solar-to-hydrogen peroxide conversion of photocatalytic carbon dots with anthraquinone: unveiling the dual role of surface functionalities, *Appl. Catal. B Environ.* 312 (2022), 121379.
 - [13] L. Zhang, P. Chen, Y. Xu, W. Nie, Y. Zhou, Enhanced photo-induced antibacterial application of graphene oxide modified by sodium anthraquinone-2-sulfonate under visible light, *Appl. Catal. B Environ.* 265 (2020), 118572.
 - [14] D. Jiang, Q. Zhang, L. Yang, Y. Deng, B. Yang, Y. Liu, C. Zhang, Z. Fu, Regulating effects of anthraquinone substituents and additives in photo-catalytic oxygenation of p-xylene by molecular oxygen under visible light irradiation, *Renew. Energy* 174 (2021) 928–938.
 - [15] M. Chen, Q. Cai, X. Chen, S. Huang, Q. Feng, T. Majima, R.J. Zeng, S. Zhou, Anthraquinone-2-sulfonate as a microbial photosensitizer and capacitor drives solar-to-N₂O production with a quantum efficiency of almost unity, *Environ. Sci. Technol.* 56 (2022) 5161–5169.
 - [16] S. Zhao, C. Chen, J. Ding, S. Yang, Y. Zang, X. Qin, X. Gao, Z. Song, N. Ren, Fabrication of AQ2S/GR composite photosensitizer for the simulated solar light-driven degradation of sulfapyridine, *Environ. Sci. Ecotechnol.* 8 (2021), 100111.
 - [17] P.R. Maddigapu, A. Bedini, C. Minerio, V. Maurino, D. Vione, M. Brigante, G. Mailhot, M. Sarakha, The pH-dependent photochemistry of anthraquinone-2-sulfonate, *Photochem. Photobiol. Sci.* 9 (2010) 323–330.
 - [18] I. Loeff, A. Treinin, H. Linschitz, Photochemistry of 9,10-anthraquinone-2-sulfonate in solution. 1. Intermediates and mechanism, *J. Phys. Chem.* 87 (1983) 2536–2544.
 - [19] I. Loeff, A. Treinin, H. Linschitz, The photochemistry of 9,10-anthraquinone-2-sulfonate in solution. 2. Effects of inorganic anions: quenching vs. radical formation at moderate and high anion concentrations, *J. Phys. Chem.* 88 (1983) 4931–4937.
 - [20] K. Zhang, K.M. Parker, Halogen radical oxidants in natural and engineered aquatic systems, *Environ. Sci. Technol.* 52 (2018) 9579–9594.
 - [21] J.E. Grebel, J.J. Pignatello, W.A. Mitch, Effect of halide ions and carbonates on organic contaminant degradation by hydroxyl radical-based advanced oxidation processes in saline waters, *Environ. Sci. Technol.* 44 (2010) 6822–6828.
 - [22] O. Cabezuolo, R. Martinez haya, N. Montes, F. Bosca, M.L. Marin, Heterogeneous riboflavin-based photocatalyst for pollutant oxidation through electron transfer processes, *Appl. Catal. B Environ.* 298 (2021), 120497.
 - [23] M.Q. Yang, N. Zhang, Y. Wang, Y.J. Xu, Metal-free, robust, and regenerable 3D graphene-organics aerogel with high and stable photosensitization efficiency, *J. Catal.* 346 (2017) 21–29.
 - [24] X. Xie, N. Zhang, Z. Tang, Y. Xu, An adaptive geometry regulation strategy for 3D graphene materials: towards advanced hybrid photocatalysts, *Chem. Sci.* 9 (2018) 8876–8882.
 - [25] M. Boota, C. Chen, M. Bécuwe, L. Miao, Y. Gogotsi, Pseudocapacitance and excellent cyclability of 2,5-dimethoxy-1,4-benzoquinone on graphene, *Energy Environ. Sci.* 9 (2016) 2586–2594.
 - [26] H. Zhang, H. Lu, J. Wang, J. Zhou, M. Sui, Cr(VI) reduction and Cr(III) immobilization by acinetobacter sp. HK-1 with the assistance of a novel quinone/graphene oxide composite, *Environ. Sci. Technol.* 48 (2014) 12876–12885.
 - [27] L. Lyu, G. Yu, L. Zhang, C. Hu, Y. Sun, 4-phenoxyphenol-functionalized reduced graphene oxide nanosheets: a metal-free fenton-like catalyst for pollutant destruction, *Environ. Sci. Technol.* 52 (2018) 747–756.
 - [28] J.-M. Yan, S.-J. Li, S.-S. Yi, B.-R. Wulan, W.-T. Zheng, Q. Jiang, Anchoring and upgrading ultrafine NiPd on room-temperature-synthesized bifunctional NH₂-N-rGO toward low-cost and highly efficient catalysts for selective formic acid dehydrogenation, *Adv. Mater.* 30 (2018), 1703038.
 - [29] H. Tetsuka, R. Asahi, A. Nagoya, K. Okamoto, I. Tajima, R. Ohta, A. Okamoto, Optically tunable amino-functionalized graphene quantum dots, *Adv. Mater.* 24 (2012) 5333–5338.
 - [30] Q. Li, X. Qin, Y. Luo, W. Lu, G. Chang, A.M. Asiri, A.O. Al-Youbi, X. Sun, One-pot synthesis of Ag nanoparticles/reduced graphene oxide nanocomposites and their application for nonenzymatic H₂O₂ detection, *Electrochim. Acta* 83 (2012) 283–287.
 - [31] Y. Zhao, H. Ding, Q. Zhong, Preparation and characterization of aminated graphite oxide for CO₂ capture, *Appl. Surf. Sci.* 258 (2012) 4301–4307.
 - [32] S. Verma, K.H. Kim, N. Kumar, S.S. Bhattacharya, M. Naushad, R.K. Dutta, Amine-amide functionalized graphene oxide sheets as bifunctional adsorbent for the removal of polar organic pollutants, *J. Hazard. Mater.* 429 (2022), 128308.
 - [33] X. Yongsheng, L. Xintong, H. Hongwei, S. Yuxiao, X. Qing, P. Wencho, Aminated N-doped graphene hydrogel for long-term catalytic oxidation in strong acidic environment, *J. Hazard. Mater.* 401 (2021), 123742.
 - [34] N. Kumar, V.C. Srivastava, Dimethyl carbonate production via transesterification reaction using nitrogen functionalized graphene oxide nanosheets, *Renew. Energy* 175 (2021) 1–13.
 - [35] S.R.M.S. Santiago, C.-H. Chang, T.-N. Lin, C.-T. Yuan, J.-L. Shen, Diethylenetriamine-doped graphene oxide quantum dots with tunable photoluminescence for optoelectronic applications, *ACS Appl. Nano Mater.* 2 (2019) 3925–3933.
 - [36] T. Ramanathan, F.T. Fisher, R.S. Ruoff, L.C. Brinson, Amino-functionalized carbon nanotubes for binding to polymers and biological systems, *Chem. Mater.* 17 (2005) 1290–1295.
 - [37] B. Sun, J. Liu, A.M. Cao, W.G. Song, D. Wang, Interfacial synthesis of ordered and stable covalent organic frameworks on amino-functionalized carbon nanotubes with enhanced electrochemical performance, *Chem. Commun.* 53 (2017) 6303–6306.
 - [38] H. Lu, H.K. Zhang, J. Wang, J.T. Zhou, Y. Zhou, A novel quinone/reduced graphene oxide composite as a solid-phase redox mediator for chemical and biological Acid Yellow 36 reduction, *RSC Adv.* 4 (2014) 47297–47303.
 - [39] Á. Tolosana-Moranchel, A. Manassero, M.L. Satuf, O.M. Alfano, J.A. Casas, A. Bahamonde, Influence of TiO₂-rGO optical properties on the photocatalytic activity and efficiency to photodegrade an emerging pollutant, *Appl. Catal. B Environ.* 246 (2019) 1–11.
 - [40] M. Misra, S.R. Chowdhury, T.I. Lee, Sunlight driven decomposition of toxic organic compound, coumarin, p-nitrophenol, and photo reduction of Cr(VI) ions, using a bridge structure of Au@CNT@TiO₂ nanocomposite, *Appl. Catal. B Environ.* 272 (2020), 118991.
 - [41] Frisch, M. J., Trucks, G. W., Schlegel, H. B., Scuseria, G. E., Robb, M. A., Cheeseman, J. R., Scalmani, G., Barone, V., Petersson, G. A., Nakatsuji, H., Li, X., Caricato, M., Marenich, A. V., Bloino, J., Janesko, B. G., Gomperts, R., Mennucci, B., Hratchian, H. P., Ortiz, J. V., Izmaylov, A. F., Sonnenberg, J. L., Williams-Young, D., Ding, F., Lipparini, F., Egidi, F., Goings, J., Peng, B., Petrone, A., Henderson, T., Ranasinghe, D., Zakrzewski, V. G., Gao, J., Rega, N., Zheng, G., Liang, W., Hada, M., Ehara, M., Toyota, K., Fukuda, R., Hasegawa, J., Ishida, M., Nakajima, T., Honda, Y., Kitao, O., Nakai, H., Vreven, T., Throssell, K., Montgomery, J. A., Jr., Peralta, J. E., Ogliaro, F., Bearpark, M. J., Heyd, J. J., Brothers, E. N., Kudin, K. N., Staroverov, V. N., Keith, T. A., Kobayashi, R., Normand, J., Raghavachari, K., Rendell, A. P., Burant, J. C., Iyengar, S. S., Tomasi, J., Cossi, M., Millam, J. M., Klene, M., Adamo, C., Cammi, R., Ochterski, J. W., Martin, R. L., Morokuma, K., Farkas, O., Foresman, J. B., Fox, D. J., Gaussian 16, Gaussian, Inc., Wallingford CT, 2016.
 - [42] G. Kresse, J. Furthmüller, Efficiency of ab-initio total energy calculations for metals and semiconductors using a plane-wave basis set, *Comput. Mater. Sci.* 6 (1996) 15–50.
 - [43] Z. Sui, Y. Cui, J. Zhu, B. Han, Preparation of three-dimensional graphene oxide-polyethylenimine porous materials as dye and gas adsorbents, *ACS Appl. Mater. Interfaces* 5 (2013) 9172–9179.
 - [44] A. Yang, J. Li, C. Zhang, W. Zhang, N. Ma, One-step amine modification of graphene oxide to get a green trifunctional metal-free catalyst, *Appl. Surf. Sci.* 346 (2015) 443–450.
 - [45] Z. Su, H. Wang, K. Tian, F. Xu, W. Huang, X. Tian, Simultaneous reduction and surface functionalization of graphene oxide with wrinkled structure by diethylenetriamine (DETA) and their reinforcing effects in the flexible poly(2-ethylhexyl acrylate) (P2EHA) films, *Compos. Part A* 84 (2016) 64–75.
 - [46] R.Y. Shi, C.P. Han, H. Duan, L. Xu, D. Zhou, H.F. Li, J.Q. Li, F.Y. Kang, B.H. Li, G. X. Wang, Redox-active organic sodium anthraquinone-2-sulfonate (AQ2S) anchored on reduced graphene oxide for high-performance supercapacitors, *Adv. Energy Mater.* 8 (2018), 1802088.
 - [47] Y. Wei, J. Wu, H. Yin, X. Shi, R. Yang, M. Dresselhaus, The nature of strength enhancement and weakening by pentagon–heptagon defects in graphene, *Nat. Mater.* 11 (2012) 759–763.
 - [48] Y. Wang, H. Cao, C. Chen, Y. Xie, H. Sun, X. Duan, S. Wang, Metal-free catalytic ozonation on surface-engineered graphene: microwave reduction and heteroatom doping, *Chem. Eng. J.* 355 (2019) 118–129.
 - [49] S. Dong, Y. Zhao, J. Yang, X. Liu, W. Li, L. Zhang, Y. Wu, J. Sun, J. Feng, Y. Zhu, Visible-light responsive PDI/rGO composite film for the photothermal catalytic degradation of antibiotic wastewater and interfacial water evaporation, *Appl. Catal. B Environ.* 291 (2021), 120127.
 - [50] L. Yang, K. Zhuo, X. Xu, Z. Zhang, Q. Du, G. Bai, J. Wang, Anthraquinone-modified nitrogen-doped graphene aerogel for boosting energy density of supercapacitors by self-matching of capacity, *Electrochim. Acta* 393 (2021), 139057.

- [51] H.-i Kim, Y. Choi, S. Hu, W. Choi, J.-H. Kim, Photocatalytic hydrogen peroxide production by anthraquinone-augmented polymeric carbon nitride, *Appl. Catal. B Environ.* 229 (2018) 121–129.
- [52] S.B. Sertkol, B. Esat, A.A. Momchilov, M.B. Yilmaz, M. Sertkol, An anthraquinone-functionalized reduced graphene oxide as electrode material for rechargeable batteries, *Carbon* 116 (2017) 154–166.
- [53] H. Dong, X.T. Guo, C. Yang, Z.Z. Ouyang, Synthesis of g-C₃N₄ by different precursors under burning explosion effect and its photocatalytic degradation for tylosin, *Appl. Catal. B Environ.* 230 (2018) 65–76.
- [54] C. Tan, X. Cao, X.-J. Wu, Q. He, J. Yang, X. Zhang, J. Chen, W. Zhao, S. Han, G.-H. Nam, M. Sindoro, H. Zhang, Recent advances in ultrathin two-dimensional nanomaterials, *Chem. Rev.* 117 (2017) 6225–6331.
- [55] S. Kang, L. Zhang, C. Yin, Y. Li, L. Cui, Y. Wang, Fast flash frozen synthesis of holey few-layer g-C₃N₄ with high enhancement of photocatalytic reactive oxygen species evolution under visible light irradiation, *Appl. Catal. B Environ.* 211 (2017) 266–274.
- [56] J. Wang, X. Duan, J. Gao, Y. Shen, X. Feng, Z. Yu, X. Tan, S. Liu, S. Wang, Roles of structure defect, oxygen groups and heteroatom doping on carbon in nonradical oxidation of water contaminants, *Water Res.* 185 (2020), 116244.
- [57] Y. Li, R. Jin, Y. Xing, J. Li, S. Song, X. Liu, M. Li, R. Jin, Macroscopic foam-like holey ultrathin g-C₃N₄ nanosheets for drastic improvement of visible-light photocatalytic activity, *Adv. Energy Mater.* 6 (2016), 1601273.
- [58] J. Wang, B. Chen, B. Xing, Wrinkles and folds of activated graphene nanosheets as fast and efficient adsorptive sites for hydrophobic organic contaminants, *Environ. Sci. Technol.* 50 (2016) 3798–3808.
- [59] A. Sumboja, C.Y. Foo, X. Wang, P.S. Lee, Large areal mass, flexible and free-standing reduced graphene oxide/manganese dioxide paper for asymmetric supercapacitor device, *Adv. Mater.* 25 (2013) 2809–2815.
- [60] M.C. Dodd, C. Huang, Aqueous chlorination of the antibacterial agent trimethoprim: reaction kinetics and pathways, *Water Res.* 41 (2007) 647–655.
- [61] Y. Lei, S.S. Cheng, N. Luo, X. Yang, T.C. An, Rate constants and mechanisms of the reactions of Cl[•] and Cl₂^{•-} with trace organic contaminants, *Environ. Sci. Technol.* 53 (2019) 11170–11182.
- [62] M.-H. Hsu, T.-H. Kuo, Y.-E. Chen, C.-H. Huang, C.-C. Hsu, A.Y.-C. Lin, Substructure reactivity affecting the manganese dioxide oxidation of cephalosporins, *Environ. Sci. Technol.* 52 (2018) 9188–9195.
- [63] P. Wardman, Reduction potentials of one-electron couples involving free-radicals in aqueous solution, *J. Phys. Chem. Ref. Data* 18 (1989) 1637–1755.
- [64] C. Sun, L. Karupppasamy, L. Gurusamy, H.-J. Yang, C.-H. Liu, J. Dong, J.J. Wu, Facile sonochemical synthesis of CdS/COF heterostructured nanocomposites and their enhanced photocatalytic degradation of Bisphenol-A, *Sep. Purif. Technol.* 271 (2021), 118873.
- [65] S.R. Yashas, H.P. Shivaraju, G. McKay, B. Shahmoradi, A. Maleki, K. Yetilmezsoy, Designing bi-functional silver delafossite bridged graphene oxide interfaces: Insights into synthesis, characterization, photocatalysis and bactericidal efficiency, *Chem. Eng. J.* 426 (2021), 131729.
- [66] A. Bedini, E. De Laurentis, B. Sur, V. Maurino, C. Minero, M. Brigante, G. Mailhot, D. Vione, Phototransformation of anthraquinone-2-sulphonate in aqueous solution, *Photochem. Photobiol. Sci.* 11 (2012) 1445–1453.
- [67] D. Dinda, H. Park, H. Lee, S. Oh, S.Y. Park, Graphene quantum dot with covalently linked Rhodamine dye: a high efficiency photocatalyst for hydrogen evolution, *Carbon* 167 (2020) 760–769.
- [68] L. Hurtado, R. Natividad, E. Torres-García, J. Farias, G. Li Puma, Correlating the photocatalytic activity and the optical properties of LiVMoO₆ photocatalyst under the UV and the visible region of the solar radiation spectrum, *Chem. Eng. J.* 262 (2015) 1284–1291.
- [69] K.M. Parker, W.A. Mitch, Halogen radicals contribute to photooxidation in coastal and estuarine waters, *Proc. Natl. Acad. Sci. USA* 113 (2016) 5868–5873.
- [70] R.E. Huie, C.L. Clifton, P. Neta, Electron transfer reaction rates and equilibria of the carbonate and sulfate radical anions, *Radiat. Phys. Chem.* 38 (1991) 477–481.
- [71] Z. Wu, J. Fang, Y. Xiang, C. Shang, X. Li, F. Meng, X. Yang, Roles of reactive chlorine species in trimethoprim degradation in the UV/chlorine process: kinetics and transformation pathways, *Water Res.* 104 (2016) 272–282.
- [72] Y. Zhou, C. Chen, K. Guo, Z. Wu, L. Wang, Z. Hua, J. Fang, Kinetics and pathways of the degradation of PPCPs by carbonate radicals in advanced oxidation processes, *Water Res.* 185 (2020), 116231.
- [73] K. Guo, Z. Wu, S. Yan, B. Yao, W. Song, Z. Hua, X. Zhang, X. Kong, X. Li, J. Fang, Comparison of the UV/chlorine and UV/H₂O₂ processes in the degradation of PPCPs in simulated drinking water and wastewater: kinetics, radical mechanism and energy requirements, *Water Res.* 147 (2018) 184–194.
- [74] G.V. Buxton, C.L. Greenstock, W.P. Helman, A.B. Ross, Critical review of rate constants for reactions of hydrated electrons, hydrogen atoms and hydroxyl radicals (•OH/•O⁻) in aqueous solution, *J. Phys. Chem. Ref. Data* 17 (1988) 513–886.
- [75] G. Liu, C. Feng, P. Shao, Degradation of perfluorooctanoic acid with hydrated electron by a heterogeneous catalytic system, *Environ. Sci. Technol.* 56 (2022) 6223–6231.
- [76] B.G. Ershov, M. Kelm, E. Janata, A.V. Gordeev, E. Bohnert, Radiation-chemical effects in the near-field of a final disposal site: role of bromine on the radiolytic processes in NaCl-solutions, *Radiochim. Acta* 90 (2002) 617–622.
- [77] A. Donati, *Spectroscopic and Kinetic Investigations of Halogen Containing Radicals in the Tropospheric Aqueous Phase*, University of Leipzig, 2002.
- [78] B.M. Matthew, C. Anastasio, A chemical probe technique for the determination of reactive halogen species in aqueous solution: part 1 – bromide solutions, *Atmos. Chem. Phys.* 6 (2006) 2423–2437.
- [79] R. Zhang, P. Sun, T. Boyer, L. Zhao, C. Huang, Degradation of pharmaceuticals and metabolite in synthetic human urine by UV, UV/H₂O₂, and UV/PDS, *Environ. Sci. Technol.* 49 (2015) 3056–3066.
- [80] J. Wenk, U. von Gunten, S. Canonica, Effect of dissolved organic matter on the transformation of contaminants induced by excited triplet states and the hydroxyl radical, *Environ. Sci. Technol.* 45 (2011) 1334–1340.
- [81] J. Wang, K. Wang, Y. Guo, J. Niu, Photochemical degradation of nebulinol in different natural organic matter solutions under simulated sunlight irradiation: kinetics, mechanism and degradation pathway, *Water Res.* 173 (2020), 115524.
- [82] Y. Lei, X. Lei, P. Westerhoff, X. Zhang, X. Yang, Reactivity of chlorine radicals (Cl[•] and Cl₂^{•-}) with dissolved organic matter and the formation of chlorinated byproducts, *Environ. Sci. Technol.* 55 (2021) 689–699.
- [83] J. Colina-Márquez, F. Machuca-Martínez, G.L. Puma, Radiation absorption and optimization of solar photocatalytic reactors for environmental applications, *Environ. Sci. Technol.* 44 (2010) 5112–5120.
- [84] G. Li Puma, A. Brucato, Dimensionless analysis of slurry photocatalytic reactors using two-flux and six-flux radiation absorption-scattering models, *Catal. Today* 122 (2007) 78–90.
- [85] G. Li Puma, V. Puddu, H.K. Tsang, A. Gora, B. Toepfer, Photocatalytic oxidation of multicomponent mixtures of estrogens (estrone (E1), 17β-estradiol (E2), 17α-ethynylestradiol (EE2) and estril (E3)) under UVA and UVC radiation: photon absorption, quantum yields and rate constants independent of photon absorption, *Appl. Catal. B Environ.* 99 (2010) 388–397.
- [86] R. Acosta-Herazo, M.Á. Mueses, G.L. Puma, F. Machuca-Martínez, Impact of photocatalyst optical properties on the efficiency of solar photocatalytic reactors rationalized by the concepts of initial rate of photon absorption (IRPA) dimensionless boundary layer of photon absorption and apparent optical thickness, *Chem. Eng. J.* 356 (2019) 839–849.
- [87] R. Acosta-Herazo, J. Monterroza-Romero, M.Á. Mueses, F. Machuca-Martínez, G. Li Puma, Coupling the Six Flux Absorption-Scattering Model to the Henyey-Greenstein scattering phase function: Evaluation and optimization of radiation absorption in solar heterogeneous photoreactors, *Chem. Eng. J.* 302 (2016) 86–96.
- [88] I. Grčić, G. Li, Puma, Six-flux absorption-scattering models for photocatalysis under wide-spectrum irradiation sources in annular and flat reactors using catalysts with different optical properties, *Appl. Catal. B Environ.* 211 (2017) 222–234.
- [89] R. Peralta Muniz Moreira, G. Li Puma, Multiphysics computational fluid-dynamics (CFD) modeling of annular photocatalytic reactors by the discrete ordinates method (DOM) and the six-flux model (SFM) and evaluation of the contaminant intrinsic kinetics constants, *Catal. Today* 361 (2021) 77–84.
- [90] A. Verma, S. Kumar, Y.-P. Fu, A ternary-hybrid as efficiently photocatalytic antibiotic degradation and electrochemical pollutant detection, *Chem. Eng. J.* 408 (2021), 127290.
- [91] X. Ma, G. Wang, L. Qin, J. Liu, B. Li, Y. Hu, H. Cheng, Z-scheme g-C₃N₄-AQ-MoO₃ photocatalyst with unique electron transfer channel and large reduction area for enhanced sunlight photocatalytic hydrogen production, *Appl. Catal. B Environ.* 288 (2021), 120025.
- [92] X. Lai, X.-a Ning, Y. Zhang, Y. Li, R. Li, J. Chen, S. Wu, Treatment of simulated textile sludge using the Fenton/Cl⁻ system: the roles of chlorine radicals and superoxide anions on PAHs removal, *Environ. Res.* 197 (2021), 110997.
- [93] J. Li, C. Ye, X. Li, Z. Li, X. Gao, B. Chen, C. Tung, L. Wu, A redox shuttle accelerates O₂ evolution of photocatalysts formed in situ under visible light, *Adv. Mater.* 29 (2017), 1606009.
- [94] J. Liang, X. Duan, X. Xu, K. Chen, F. Wu, H. Qiu, C. Liu, S. Wang, X. Cao, Biomass-derived pyrolytic carbons accelerated Fe(III)/Fe(II) redox cycle for persulfate activation: pyrolysis temperature-dependent performance and mechanisms, *Appl. Catal. B Environ.* 297 (2021), 120446.
- [95] K. Hasegawa, P. Neta, Rate constants and mechanisms of reaction of chloride (Cl₂^{•-}) radicals, *J. Phys. Chem.* 82 (1978) 854–857.
- [96] R. Zhang, Y. Yang, C.-H. Huang, N. Li, H. Liu, L. Zhao, P. Sun, UV/H₂O₂ and UV/PDS treatment of trimethoprim and sulfamethoxazole in synthetic human urine: transformation products and toxicity, *Environ. Sci. Technol.* 50 (2016) 2573–2583.
- [97] Z. Cai, Y. Song, X. Jin, C. Wang, H. Ji, W. Liu, X. Sun, Highly efficient AgBr/h-MoO₃ with charge separation tuning for photocatalytic degradation of trimethoprim: mechanism insight and toxicity assessment, *Sci. Total Environ.* 781 (2021), 146754.
- [98] H. Li, S. Sun, H. Ji, W. Liu, Z. Shen, Enhanced activation of molecular oxygen and degradation of tetracycline over Cu-S₄ atomic clusters, *Appl. Catal. B Environ.* 272 (2020), 118966.
- [99] X. Yang, X. Ding, L. Zhou, Y. Ji, G. Xiu, Oxygen dependent oxidation of trimethoprim by sulfate radical: kinetic and mechanistic investigations, *Chin. Chem. Lett.* 32 (2021) 3164–3168.
- [100] Q. Zhao, Q. Fang, H.Y. Liu, Y.J. Li, H.S. Cui, B.J. Zhang, S.L. Tian, Halide-specific enhancement of photodegradation for sulfadiazine in estuarine waters: roles of halogen radicals and main water constituents, *Water Res.* 160 (2019) 209–216.
- [101] C. Chen, Z. Wu, S. Hou, A. Wang, J. Fang, Transformation of gemfibrozil by the interaction of chloride with sulfate radicals: radical chemistry, transient intermediates and pathways, *Water Res.* 209 (2022), 117944.
- [102] M. Hayyan, M.A. Hashim, I.M. AlNashef, Superoxide ion: generation and chemical implications, *Chem. Rev.* 116 (2016) 3029–3085.
- [103] S. Xie, C. Tang, H. Shi, G. Zhao, Highly efficient photoelectrochemical removal of atrazine and the mechanism investigation: bias potential effect and reactive species, *J. Hazard. Mater.* 415 (2021), 125681.

- [104] J. Yang, H. Miao, J. Jing, Y. Zhu, W. Choi, Photocatalytic activity enhancement of PDI supermolecular via π - π action and energy level adjusting with graphene quantum dots, *Appl. Catal. B Environ.* 281 (2021), 119547.
- [105] X. Li, J. Chen, X. Wang, J. Sun, M. Antonietti, Metal-free activation of dioxygen by graphene/g-C₃N₄ nanocomposites: functional dyads for selective oxidation of saturated hydrocarbons, *J. Am. Chem. Soc.* 133 (2011) 8074–8077.
- [106] R.S. Mulliken, Electronic population analysis on LCAO–MO molecular wave functions. I, *J. Chem. Phys.* 23 (1955) 1833–1840.
- [107] Q. Lang, Y. Chen, T. Huang, L. Yang, S. Zhong, L. Wu, J. Chen, S. Bai, Graphene “bridge” in transferring hot electrons from plasmonic Ag nanocubes to TiO₂ nanosheets for enhanced visible light photocatalytic hydrogen evolution, *Appl. Catal. B: Environ.* 220 (2018) 182–190.
- [108] J. Zhang, R. Balasubramanian, X. Yang, Novel 3D multi-layered carbon nitride/indium sulfide heterostructure for boosted superoxide anion radical generation and enhanced photocatalysis under visible light, *Chem. Eng. J.* 453 (2023), 139776.